


## Article

# A Cellulose-Derived Nanofibrous MnO<sub>2</sub>-TiO<sub>2</sub>-Carbon Composite as Anodic Material for Lithium-Ion Batteries

Shun Li <sup>1,2,\*</sup>, Ming Yang <sup>1</sup>, Guijin He <sup>1</sup>, Dongmei Qi <sup>3</sup> and Jianguo Huang <sup>1,\*</sup> 

<sup>1</sup> Department of Chemistry, Zhejiang University, Hangzhou 310027, China; 21937064@zju.edu.cn (M.Y.); guikinghe@zju.edu.cn (G.H.)

<sup>2</sup> School of Engineering, Zhejiang Agriculture and Forestry University, Hangzhou 311300, China

<sup>3</sup> Analysis Center of Agrobiological and Environmental Sciences, Zhejiang University, Hangzhou 310027, China; qidongmei@zju.edu.cn

\* Correspondence: smoothlee2013@zju.edu.cn (S.L.); jghuang@zju.edu.cn (J.H.); Tel.: +86-571-8795-1202 (J.H.)

**Abstract:** A bio-inspired nanofibrous MnO<sub>2</sub>-TiO<sub>2</sub>-carbon composite was prepared by utilizing natural cellulosic substances (e.g., ordinary quantitative ashless filter paper) as both the carbon source and structural matrix. Mesoporous MnO<sub>2</sub> nanosheets were densely immobilized on an ultrathin titania film precoated with cellulose-derived carbon nanofibers, which gave a hierarchical MnO<sub>2</sub>-TiO<sub>2</sub>-carbon nanoarchitecture and exhibited excellent electrochemical performances when used as an anodic material for lithium-ion batteries. The MnO<sub>2</sub>-TiO<sub>2</sub>-carbon composite with a MnO<sub>2</sub> content of 47.28 wt % exhibited a specific discharge capacity of 677 mAh g<sup>-1</sup> after 130 repeated charge/discharge cycles at a current rate of 100 mA g<sup>-1</sup>. The contribution percentage of MnO<sub>2</sub> in the composite material is equivalent to 95.1% of the theoretical capacity of MnO<sub>2</sub> (1230 mAh g<sup>-1</sup>). The ultrathin TiO<sub>2</sub> precoating layer with a thickness ca. 2 nm acts as a crucial interlayer that facilitates the growth of well-organized MnO<sub>2</sub> nanosheets onto the surface of the titania-carbon nanofibers. Due to the interweaved network structures of the carbon nanofibers and the increased content of the immobilized MnO<sub>2</sub>, the exfoliation and aggregation, as well as the large volume change of the MnO<sub>2</sub> nanosheets, are significantly inhibited; thus, the MnO<sub>2</sub>-TiO<sub>2</sub>-carbon electrodes displayed outstanding cycling performance and a reversible rate capability during the Li<sup>+</sup> insertion/extraction processes.

**Keywords:** bio-inspired materials; cellulosic substances; titania film; MnO<sub>2</sub> nanosheets; lithium-ion batteries



**Citation:** Li, S.; Yang, M.; He, G.; Qi, D.; Huang, J. A Cellulose-Derived Nanofibrous MnO<sub>2</sub>-TiO<sub>2</sub>-Carbon Composite as Anodic Material for Lithium-Ion Batteries. *Materials* **2021**, *14*, 3411. <https://doi.org/10.3390/ma14123411>

Academic Editor: Halina Kaczmarek

Received: 31 May 2021

Accepted: 17 June 2021

Published: 20 June 2021

**Publisher's Note:** MDPI stays neutral with regard to jurisdictional claims in published maps and institutional affiliations.



**Copyright:** © 2021 by the authors. Licensee MDPI, Basel, Switzerland. This article is an open access article distributed under the terms and conditions of the Creative Commons Attribution (CC BY) license (<https://creativecommons.org/licenses/by/4.0/>).

## 1. Introduction

Lithium-ion batteries (LIBs) are regarded as one of the most practical and effective technologies for the development of electric vehicles, mobile devices, and reproducible energy integration [1,2]. The key points to boost the power and energy density of LIBs largely rely on the physiochemical properties of the anodic and cathodic materials [3,4]. Traditionally adopted commercial graphite anode materials deliver a relatively low specific capacity of 372 mAh g<sup>-1</sup>, which are unable to satisfy the increasing requirements for high energy storage [5]. Compared with conventional commercialized graphite anodes, transition metal oxides have caused a great deal of interest thanks to their high theoretical capacities and reliable discharging rates [6–11]. Among the various transition metal oxides, manganese oxide (MnO<sub>2</sub>) is an attractive electrode candidate for LIBs due to its high storage capacity (1230 mAh g<sup>-1</sup>), rich abundance, and environmental friendliness [12,13]. However, the practical applications of MnO<sub>2</sub>-based anode materials are greatly limited by their poor intrinsic electric conductivity (~10<sup>-7</sup>–10<sup>-8</sup> S cm<sup>-1</sup>) and severe volume expansion and pulverization of MnO<sub>2</sub> matter from repeated charge/discharge cycles [14,15].

To overcome these issues, many attempts have been made to increase the capacity stability and the electric conductivity of MnO<sub>2</sub>-based anode materials. An effective approach is the construction of nanoarchitectures with new composites composed of electrically

conductive carbon or graphite and  $\text{MnO}_2$  so as to enhance the electrochemical performance of the anode materials [16]. For example, a curly  $\text{MnO}_2$  nanoflake electrode delivered a reversible capacity of  $696 \text{ mAh g}^{-1}$  as the cycling rate returned to  $50 \text{ mA g}^{-1}$ , which was ascribed to its high surface-to-volume ratio and stable structure [17]. A coaxial  $\text{MnO}_2/\text{CNT}$  array composite material delivered a first discharge capacity of ca.  $2000 \text{ mAh g}^{-1}$  at a current rate of  $50 \text{ mA g}^{-1}$ . Unfortunately, the capacity suddenly dropped to  $500 \text{ mAh g}^{-1}$  after 15 cycles. The fast degradation of the  $\text{MnO}_2/\text{CNT}$  materials was due to the structural destruction of the thick  $\text{MnO}_2$  layer deposited on the outer surface of the CNTs [18]. It has also been demonstrated that carbon nanohorns (CNHs) possess good electric conductivity and a large surface area and acted as a carrier for  $\text{MnO}_2$  nanosheets; the composite showed a reversible discharge capacity of  $565 \text{ mAh g}^{-1}$  as tested at a 0.1-C current rate ( $1 \text{ C} = 1000 \text{ mA g}^{-1}$ ) after 60 charge/discharge cycles [19]. Moreover, a layer-by-layer graphene- $\text{MnO}_2$  nanotube composite exhibited a reversible capacity of  $495 \text{ mAh g}^{-1}$  after 40 cycles at a rate of  $100 \text{ mA g}^{-1}$  [20]. However, these  $\text{MnO}_2$ -based electrode materials showed rapid capacity degradation and failed to realize satisfactory cycling performance and reversible rate capability.

$\text{TiO}_2$  has been explored as an active anodic material for LIBs owing to its attractive properties, such as its low cost, safety, and relatively low volume expansion during the charge/discharge processes. The excellent physicochemical characteristics of  $\text{TiO}_2$  lead to the long cycling life and durability of the electrodes. However, the low theoretical capacity of around  $335 \text{ mAh g}^{-1}$  and the inherently slow transport kinetics for both Li ions and electrons severely hinder  $\text{TiO}_2$ 's practical application [21,22]. Various nanostructured  $\text{TiO}_2$  and  $\text{TiO}_2$ -based carbon composites have been developed, aiming at improving the ionic and electric transportation of electrodes during Li/Li<sup>+</sup> processes [23]. A bio-inspired multilevel nanofibrous silver-nanoparticle-anatase-rutile-titania composite material, which was composed of anatase-phase titania nanotubes with rutile-phase titania and further immobilized with silver nanoparticles, displayed a stable capacity of  $120 \text{ mAh g}^{-1}$  after 100 cycles, with a Coulombic efficiency of approximately 100% [24]. Moreover, it was also confirmed that nanofibrous  $\text{TiO}_2$ -coated carbon composites deposited with silver nanoparticles exhibited an initial discharge capacity of  $1323 \text{ mAh g}^{-1}$  and maintained  $320 \text{ mAh g}^{-1}$  in the first 150 cycles when employed as anodes for LIBs [25]; however, these  $\text{TiO}_2$ -related anode materials failed to achieve a high capacity and capacity retention.

The biomimetic synthesis approach is believed to be an effective way to fabricate functional nanomaterials with specific structure morphologies and to design physicochemical properties that are faithfully inherited from an original biological organism [26–30]. Natural cellulose substances, which possess unique interwoven network structures, are verified to be a desirable structural matrix and template for the self-assembly of active guest components on their surfaces through a layer-by-layer method, which shows great potential in the fabrication of cellulose-derived materials for lithium-ion batteries. The hierarchical porous structures of cellulose substance-derived functional nanomaterials are unique [31], and cannot be obtained using other synthesis method, such as the combination of different nanoscale building blocks [16]. Herein, a bio-inspired nanofibrous  $\text{MnO}_2\text{-TiO}_2$ -carbon composite was prepared by employing natural cellulose substances (commercial laboratory filter paper) as both the carbon source and the structural matrix using a facile sol-gel process and hydrothermal procedures. The carbon nanofibers were deposited on an ultrathin  $\text{TiO}_2$  layer and additional  $\text{MnO}_2$  nanosheets were then immobilized to construct the  $\text{MnO}_2\text{-TiO}_2$ -carbon nanoarchitecture. The three-dimensional network structure of the composite material was fully inherited from the initial cellulosic substances. In addition, the titania precoating interlayer greatly contributed to the well-organized immobilization, as well as to the higher loading of content of the porous  $\text{MnO}_2$  nanosheets. The  $\text{MnO}_2\text{-TiO}_2$ -carbon material displayed preeminent cycling stabilities and reversible rate capabilities when utilized as an anodic material for LIBs. The improvement of the electrochemical capabilities of the nanocomposite were ascribed to the distinct interconnected structures and the high surface-to-volume ratio of the carbon matrix, which significantly alleviated

the volumetric expansion and agglomeration of the anode material upon cycling. Moreover, the carbon scaffold also acted as a conductive matrix and facilitated fast  $\text{Li}^+$  and ion transport in the  $\text{Li}/\text{Li}^+$  processes. The titania thin film also contributed to the strong adhesion between the carbon nanofiber and the  $\text{MnO}_2$  nanosheets, and suppressed the pulverization and exfoliation of the  $\text{MnO}_2$  nanosheets from the  $\text{MnO}_2$ - $\text{TiO}_2$ -carbon material. Due to the synergetic effect of the three components, the  $\text{MnO}_2$ - $\text{TiO}_2$ -carbon anode material exhibited improved electrochemical performance.

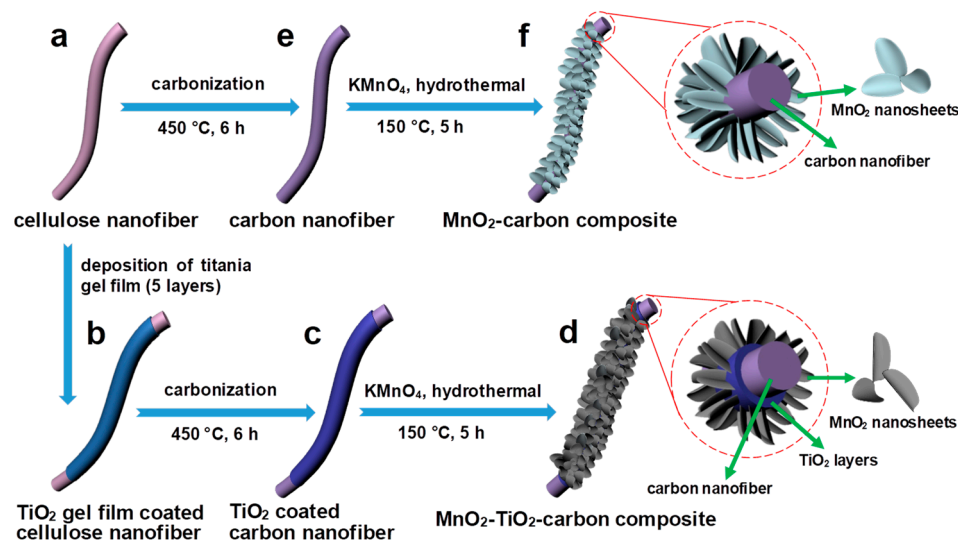
## 2. Materials and Methods

### 2.1. Materials

Ordinary quantitative ashless filter paper was obtained from Hangzhou Xinhua Paper Industry Co. Ltd. (Hangzhou, China). Potassium permanganate ( $\text{KMnO}_4$ , >99%) was bought from Sigma Aldrich (St. Louis, MO, USA). Other chemical reagents used in the experiments were acquired and employed without additional treatment. DI water was utilized in all fabrication processes and was purified using a Milli-Q Advantage A10 system (Millipore, Bedford, MA, USA) with a given electrical resistance of over 18.2  $\text{M}\Omega$  cm.

### 2.2. Fabrication of the Nanofibrous $\text{MnO}_2$ - $\text{TiO}_2$ -Carbon and $\text{MnO}_2$ -Carbon Composites

In a representative procedure, 5-layer titania gel film was deposited onto the surface of cellulose nanofibers from bulk quantitative filter paper using a surface sol-gel method (Scheme 1a,b), which was followed by carbonization of the as-synthesized  $\text{TiO}_2$  gel film by precoating the cellulose nanofiber in an Ar atmosphere at 450 °C for 6 h to obtain the  $\text{TiO}_2$ -carbon nanocomposite (Scheme 1c) [25]. Subsequently, 20.0 mg of  $\text{TiO}_2$ -carbon material was added into 20 mL DI water with sonification for 1.5 h, in order to control the  $\text{MnO}_2$  content in the resultant composite. Various weights of  $\text{KMnO}_4$  (30 and 25 mg) were then added and stirred under the ambient temperature for 5 h. Finally, the two as-obtained violet mixtures were transferred to 50-mL Teflon-lined autoclaves (Zhongnuo Instrument Co., Ltd., Xi'an, China), respectively, and further heated in a muffle furnace (Jinghong Experimental Equipment Co., Ltd., Shanghai, China) at 150 °C for 5 h. After cooling to an ambient temperature, the brownish products were rinsed with DI water and absolute ethanol 3–4 times, and were dried further overnight in an electric vacuum oven (80 °C, Yiheng Scientific Instrument Co., Ltd., Shanghai, China) (Scheme 1d). As verified by thermal gravimetric analyses (TGA), the contents of  $\text{MnO}_2$  in the  $\text{MnO}_2$ - $\text{TiO}_2$ -carbon composites were measured to be 47.28 wt % and 37.81 wt %, respectively. The corresponding composites were designated as  $\text{MnO}_2$ - $\text{TiO}_2$ -carbon-47.28% and  $\text{MnO}_2$ - $\text{TiO}_2$ -carbon-37.81%, respectively. As for the control experiment,  $\text{MnO}_2$ -carbon materials with varying  $\text{MnO}_2$  contents were fabricated under same conditions without a pre-deposited titania gel layer (Scheme 1e,f). The TGA measurements showed that the  $\text{MnO}_2$  contents in the  $\text{MnO}_2$ -carbon composite were 40.15 wt % and 33.30 wt % when the addition of  $\text{KMnO}_4$  was 30 and 25 mg, respectively. The obtained composites were designated as  $\text{MnO}_2$ -carbon-40.15% and  $\text{MnO}_2$ -carbon-33.30%, respectively. The  $\text{MnO}_2$  nanoparticles ( $\text{MnO}_2$ -NPs) were fabricated by the addition of 0.2 g  $\text{KMnO}_4$  and 0.2 mL  $\text{H}_2\text{SO}_4$  (95 wt %) to 25 mL DI water to form a precursor, and followed by hydrothermal reaction at 150 °C for 4 h.



**Scheme 1.** Schematic illustration of the fabrication processes of the MnO<sub>2</sub>-TiO<sub>2</sub>-carbon (a–d) and MnO<sub>2</sub>-carbon (a–f) composites derived from natural cellulosic substances. (b) The TiO<sub>2</sub> gel film coated cellulose nanofiber was obtained by means of a surface sol–gel process. (c) The TiO<sub>2</sub> coated carbon nanofiber and (e) the carbon nanofiber were fabricated through carbonization of the TiO<sub>2</sub> gel film coated cellulose nanofiber and the cellulose nanofiber in an argon atmosphere, respectively. (d) MnO<sub>2</sub>-TiO<sub>2</sub>-carbon and (f) MnO<sub>2</sub>-carbon were fabricated via a hydrothermal process by employing KMnO<sub>4</sub> as precursor.

### 2.3. Characterizations

A small amount of specimen was dispersed in absolute ethanol followed by ultrasonication for 60 s; then, the suspensions were dropped onto aluminum foil for field emission scanning electron microscopy (FE-SEM) tests on a Hitachi SU-8010 (HITACHI, Tokyo, Japan) instrument with an acceleration voltage of 5.0 kV. In the meantime, the resultant mixtures were placed on a copper grid for transmission electron microscopy (TEM) observations on a Hitachi HT-7700 (HITACHI, Tokyo, Japan) tool with an acceleration voltage of 100 kV. High-resolution transmission electron microscopy (HR-TEM) and selected area electron diffraction (SAED) measurements were conducted on a JEM-2100F apparatus (JEOL, Tokyo, Japan) with an acceleration voltage of 300 kV. X-ray diffraction (XRD) measurements were performed on a Philips X'Pert PRO diffractometer (PANalytical B.V., Alemlo, The Netherlands) using CuK $\alpha$  ( $\lambda = 0.15405$  nm) as a radiant source. X-ray photoelectron spectra (XPS) were detected by employing a VG Escalab Mark 2 spectrophotometer (VG Instruments, Manchester, UK) with a MgK $\alpha$  X-ray source (1253.6 eV). High-resolution scans of Mn were performed at 0.2 eV increments (sweep time: 1000 ms eV<sup>-1</sup>, each region: 30 energy sweeps). The C 1s peak at 284.50 eV was used as a standard for all the XPS peaks. Raman spectra were obtained using a Jobin Yvon LabRam HR UV Raman spectrometer (HORIBA, Paris, France) with an excitation wavelength of 532 nm. Thermal gravimetric analyses (TGA) were performed on a Mettler Toledo STARe System TGA2 (Mettler Toledo Crop., Zurich, Switzerland) at a heating rate of 10 °C min<sup>-1</sup>, from room temperature to 800 °C in a nitrogen atmosphere. The specific surface areas of the samples were determined through measurement of the N<sub>2</sub> adsorption–desorption isotherms at –196 °C with a Micromeritics ASAP-2020 tool (Micromeritics, Norcross, GA, USA), and the Brunauer–Emmett–Teller (BET) method was applied to compute the surface area and pore volume of the MnO<sub>2</sub>-TiO<sub>2</sub>-carbon composites.

### 2.4. Electrochemical Measurements

The working electrodes were prepared by mixing Super P (10 wt %) and polyvinylidene fluoride binder (PVDF, 10 wt %) with the active material (80 wt %) in *N*-methyl-2-pyrrolidinone (NMP) solvent. The slurries were uniformly coated onto copper foam

and dried in a vacuum oven (80 °C, 12 h); the electrodes were then pressed at 12 atm and the mass loading of the active material was ca. 1.5–2.0 mg for each electrode. Coin-type cells (CR2025, DodoChem, Suzhou, China) were assembled in an argon filled glove box with concentrations of oxygen and water molecules less than 0.1 ppm. A Li metal plate was used as the auxiliary electrode and polypropylene (Celglad 2300, DodoChem, Suzhou, China) film was used as the separator. The electrolyte was composed of 1.0 M LiPF<sub>6</sub> in ethylene carbonate (EC), ethyl methyl carbonate (EMC), and dimethyl carbonate (DMC) (EC:EMC:DMC, v:v:v = 1:1:1). Cyclic voltammetry (CV) tests were performed on a CHI760D electrochemical workstation (CH instruments, Shanghai, China) with a scan rate of 0.1 mV s<sup>-1</sup> and voltage window of 0.01–3.0 V. Galvanostatic charge/discharge performances were tested using a Neware battery testing system (Neware Technology Co., Ltd., Shenzhen, China) in the voltage range from 0.01 to 3.0 V (Li/Li<sup>+</sup>) at ambient temperature. Electrochemical impedance spectra (EIS) measurements were recorded in the frequency range of 100 kHz to 0.01 Hz. The structural stability of the electrode composites after 200 charge/discharge cycles was confirmed via electron microscope observations.

### 3. Results and Discussion

#### 3.1. Structural Characterizations of the MnO<sub>2</sub>-TiO<sub>2</sub>-Carbon and MnO<sub>2</sub>-Carbon Composites

As illustrated in Scheme 1, the MnO<sub>2</sub>-based carbon composites were obtained by utilizing natural cellulosic substances (e.g., common commercial filter paper) as both the scaffolds and carbon sources. The MnO<sub>2</sub> nanosheets were uniformly immobilized on the surfaces of the ultrathin TiO<sub>2</sub>-coated carbon nanofibers or on the nanofibrous carbon to acquire MnO<sub>2</sub>-TiO<sub>2</sub>-carbon (Scheme 1a–d) and MnO<sub>2</sub>-carbon composites (Scheme 1a–f). The resultant materials with varied MnO<sub>2</sub> contents were denoted as MnO<sub>2</sub>-TiO<sub>2</sub>-carbon-47.28%, MnO<sub>2</sub>-TiO<sub>2</sub>-carbon-37.81%, MnO<sub>2</sub>-carbon-40.15%, and MnO<sub>2</sub>-carbon-33.30%, respectively.

The morphology and structure properties of the MnO<sub>2</sub>-TiO<sub>2</sub>-carbon-47.28% composite are shown in Figure 1. It can be clearly seen that the composite is composed of interconnected microfibrils, and each microfibril consists of nanofiber assemblies with a diameter range from tens of to several hundred nanometers (Figure 1a). The three-dimensional network structures of the nanocomposite were perfectly inherited from the original cellulose substances, and the closely-packed MnO<sub>2</sub> sheets (thickness ca. 20 nm) were evenly immobilized on the surfaces of the titania-coated carbon nanofibers (Figure 1b). The diameter of an individual MnO<sub>2</sub>-TiO<sub>2</sub>-carbon-47.28% nanofiber isolated from the nanofiber assemblies was ca. 400 nm (Figure 1c). A high-magnification TEM image (Figure 1d) of the composite nanofiber shows MnO<sub>2</sub> nanosheets with a pore structure that was formed from the evaporation of the H<sub>2</sub>O molecules.

The selected area electron diffraction (SAED) of an individual MnO<sub>2</sub>-TiO<sub>2</sub>-carbon-47.28% nanofiber and the relevant EDS elemental mapping of carbon (C), titanium (Ti), oxygen (O), manganese (Mn) are shown in Figure 2. It was observed that C appears in the central area of the composite nanofiber, whereas the distribution zones of Mn and O were comparable and wider than those of Ti and C. This implies that the MnO<sub>2</sub> nanosheets were uniformly immobilized on the surface of the titania-coated carbon nanofibers. In comparison, the multilevel structures of original filter paper were perfectly sustained by the resultant MnO<sub>2</sub>-TiO<sub>2</sub>-carbon-37.81% composite (Figure S1, Supplementary Materials). The densely loaded MnO<sub>2</sub> nanosheets (thickness ca. 15 nm) were anchored to the surface of the titania-carbon nanofibers, and MnO<sub>2</sub> nanorods with a diameter of around 20 nm were connected by the adjacent MnO<sub>2</sub>-TiO<sub>2</sub>-carbon-37.81% composite nanofibers to construct three-dimensional cross-linked network structures. When these two composites were tested as anode materials for LIBs, the MnO<sub>2</sub>-TiO<sub>2</sub>-carbon-47.28% composite showed a higher electrochemical performance than the sample MnO<sub>2</sub>-TiO<sub>2</sub>-carbon-37.81%. This was attributed to the stronger binding force between the well-organized MnO<sub>2</sub> nanosheets and the titania coating layer in MnO<sub>2</sub>-TiO<sub>2</sub>-carbon-47.28%. Hence, the large volume change and pulverization of the MnO<sub>2</sub> nanosheets were significantly alleviated.

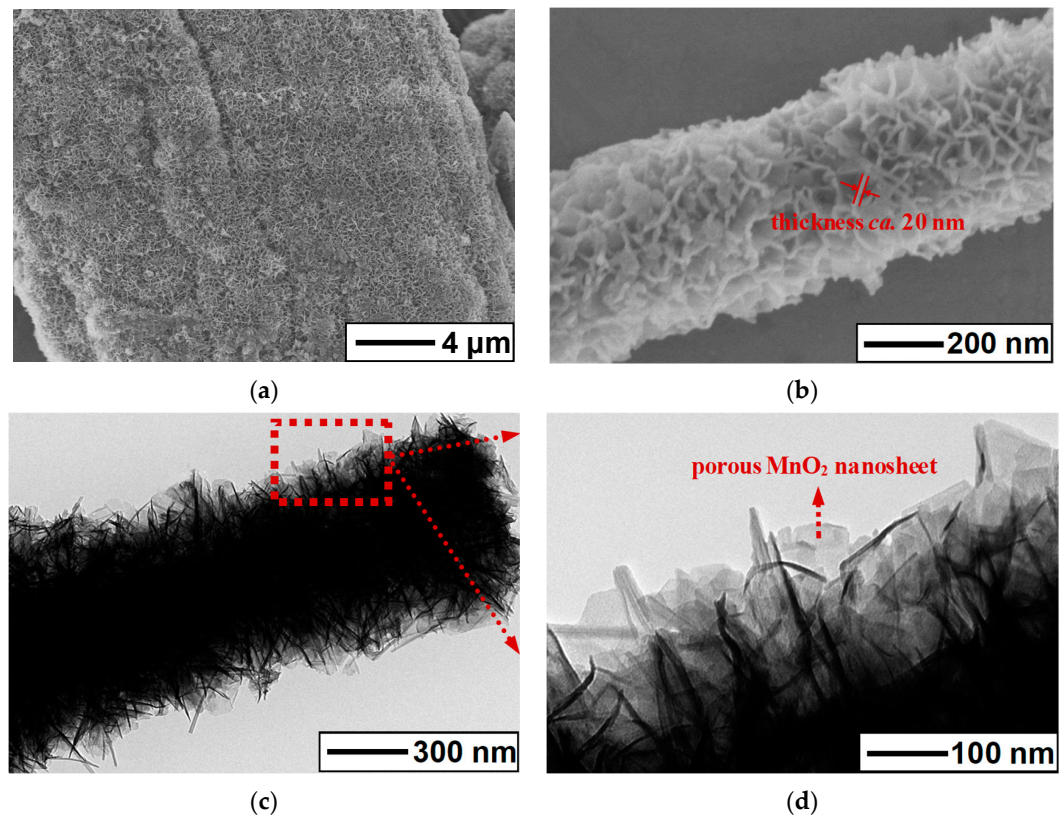


**Figure 1.** Electron micrographs of the cellulose-derived  $\text{MnO}_2$ - $\text{TiO}_2$ -carbon-47.28% composite. (a) FE-SEM image of the composite showing nanofiber assemblies; (b) an individual composite material separated from the assemblies; (c) TEM image of an individual  $\text{MnO}_2$ - $\text{TiO}_2$ -carbon-47.28% composite; (d) partially magnified TEM image (marked by the red frame) showing the  $\text{MnO}_2$  nanosheets with porous structures.

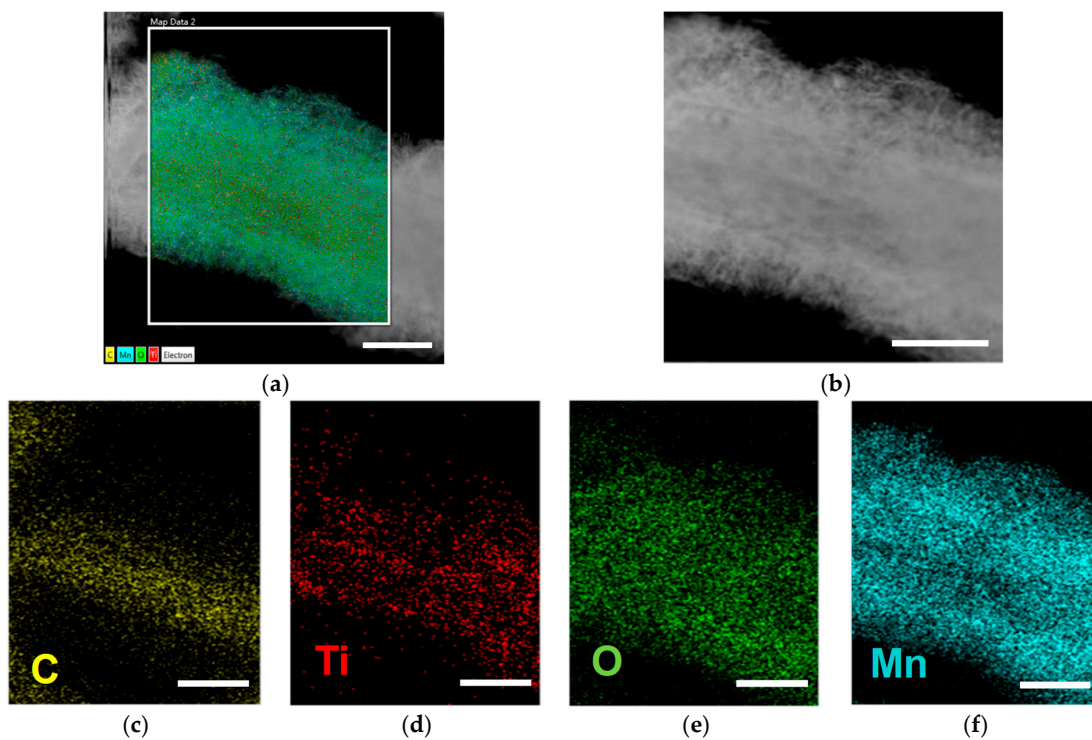


**Figure 2.** (a,b) STEM images of an individual  $\text{MnO}_2$ - $\text{TiO}_2$ -carbon-47.28% composite nanofiber with the corresponding EDS elemental mapping of (c) C, (d) Ti, (e) O and (f) Mn. Scale bars = 500 nm.

Figure 3 shows SEM and TEM images of the MnO<sub>2</sub>-carbon-40.15% composite, extensive MnO<sub>2</sub> nanosheets and a few MnO<sub>2</sub> nanorods grew on the surfaces of the nanofibrous carbon (Figure 3a,b). The immobilized MnO<sub>2</sub> nanosheets with a porous structure can obviously be seen in Figure 3c,d. In contrast, the density of the MnO<sub>2</sub> nanosheets in MnO<sub>2</sub>-carbon-40.15% was lower than that of the MnO<sub>2</sub>-TiO<sub>2</sub>-carbon-47.28% composite because the titania film provided more active sites for the growth of MnOOH, which resulted in the well-organized growth of MnO<sub>2</sub> nanosheets of smaller sizes [32]. The original multilevel morphology of the structures can still be observed in the MnO<sub>2</sub>-carbon-33.30% materials (Figure S2), showing that the closely packed MnO<sub>2</sub> nanosheets are immobilized on the surface of carbon nanofibers, crosslinked MnO<sub>2</sub> nanorods are intertwined among the MnO<sub>2</sub>-carbon-33.30% nanofibers surfaces. However, the as-fabricated MnO<sub>2</sub>-NPs with a mean diameter of ca. 30 nm and length of hundreds of nanometers tended to aggregate (Figure S3).

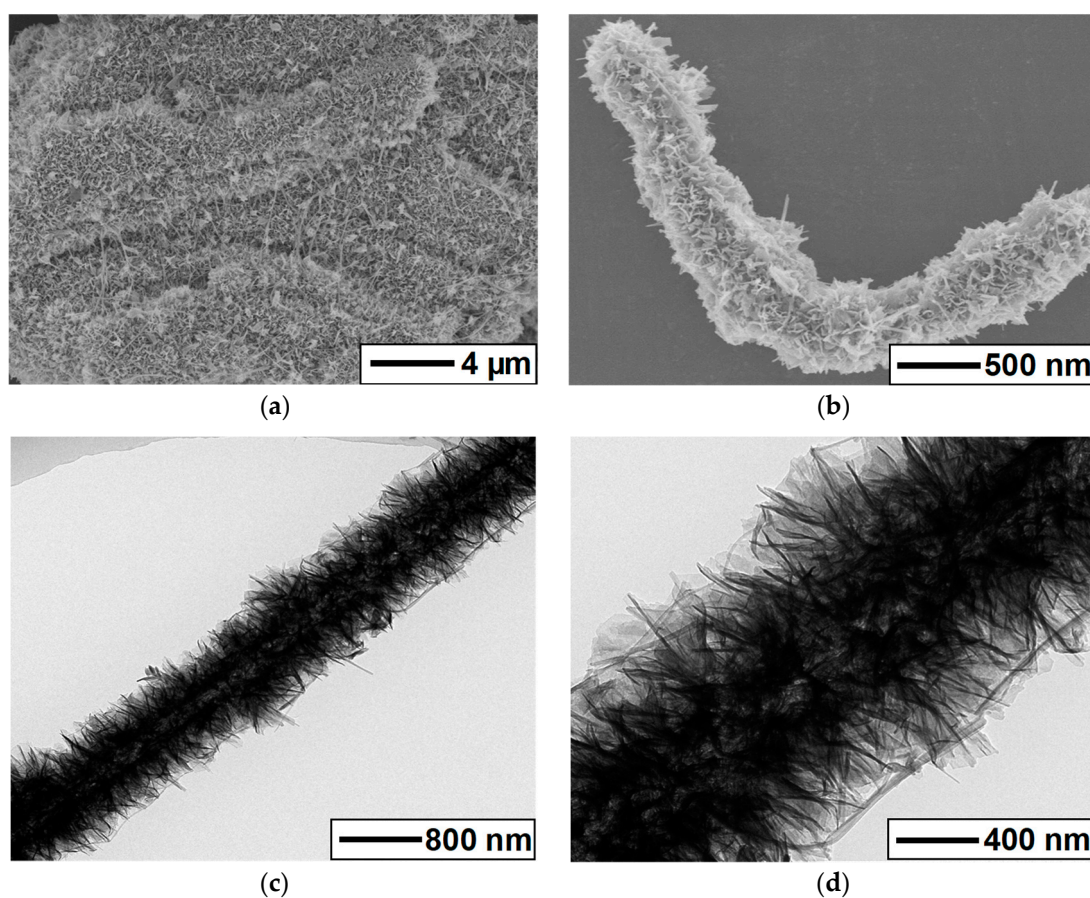


**Figure 3.** Electron micrographs of the MnO<sub>2</sub>-carbon-40.15% nanocomposite derived from a natural cellulose substance. (a) FE-SEM image of the sample, displaying nanofiber assemblies. (b) An individual composite nanofiber isolated from the assemblies. (c,d) The TEM images of an individual MnO<sub>2</sub>-carbon-40.15% nanofiber at different magnifications.

Energy-dispersive X-ray spectrometry (EDS) mapping test results are exhibited in Figure 4 to further verify the structural and elemental construction of the MnO<sub>2</sub>-carbon-40.15% materials. The uniform distributions of Mn and O elements indicate the successful immobilization of MnO<sub>2</sub> onto the surface of the carbon nanofiber (Figure 4d–f). The growth of MnO<sub>2</sub> in the MnO<sub>2</sub>-TiO<sub>2</sub>-carbon and MnO<sub>2</sub>-carbon composites are based on the following reaction [33]:



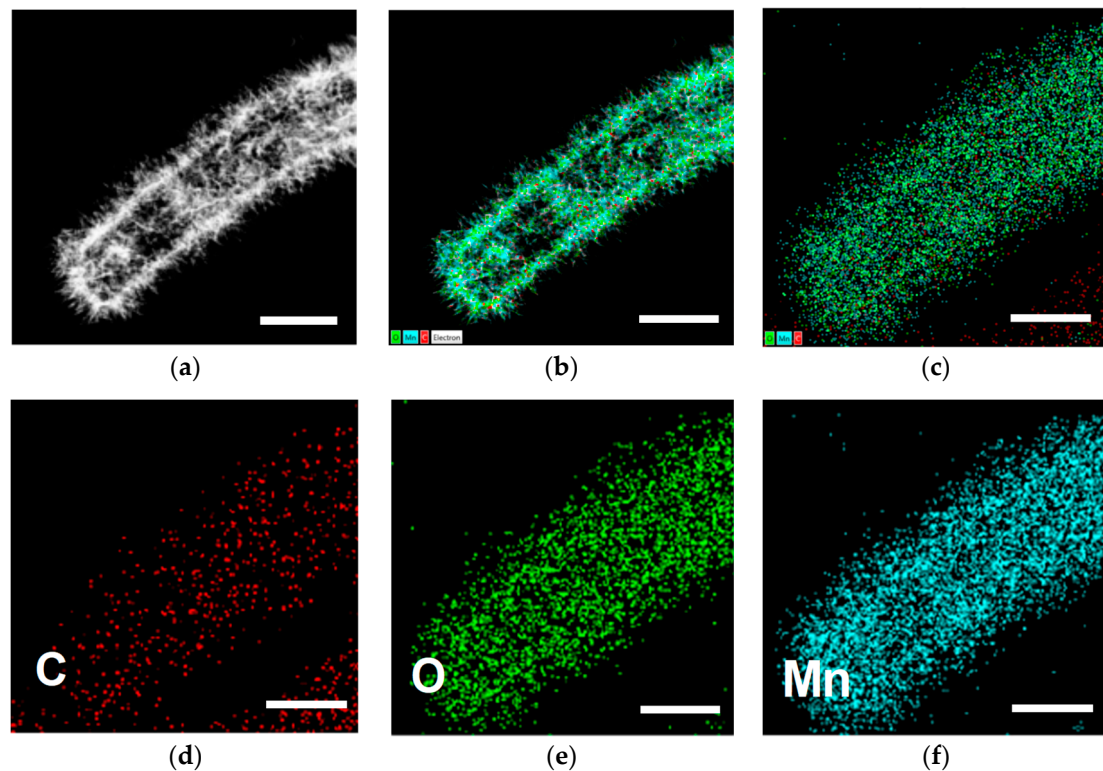


**Figure 4.** (a–c) STEM images of an individual  $\text{MnO}_2$ -carbon-40.15% composite with the corresponding EDS elemental mapping of (d) C, (e) O, and (f) Mn. Scale bars = 300 nm.

In this process, the carbon can easily react with  $\text{KMnO}_4$  in solutions and form a strong adhesion force between the  $\text{MnO}_2$  sheets and the titania-coated carbon or the carbon nanofibers. The content of  $\text{MnO}_2$  in the  $\text{MnO}_2$ - $\text{TiO}_2$ -carbon-47.28% exceeded that of the  $\text{MnO}_2$ -carbon-40.15% composite, which was due to the protective effects of the titania pre-coating layer. The interconnected carbon nanofibers derived from the natural cellulose substance served as a conductive matrix to enhance electron transportation and shorten the pathway of  $\text{Li}^+$  during cycling. In addition, the ultrathin  $\text{TiO}_2$  coating layer well facilitated the growth of  $\text{MnO}_2$  nanosheets on the surface of  $\text{TiO}_2$ -carbon nanofibers through a redox reaction, as mentioned above.

To determine the phase structure of the composite materials, Figure 5a shows the X-ray diffraction results of the corresponding samples; the major peaks presented in the  $\text{MnO}_2$ - $\text{TiO}_2$ -carbon-47.28%, 37.81%, and  $\text{MnO}_2$ -carbon-40.15%, 33.30% materials are indexed to the (001), (002), (−111) and (020) planes of  $\alpha$ - $\text{MnO}_2$  crystal (JCPDS#. 80-1098) [34]. A broad diffraction peak situated at approximately  $26^\circ$  corresponded to the (002) plane of graphitic carbon in the  $\text{TiO}_2$ -carbon composite, and the relatively weak peak intensity of the carbon reflection was seen in  $\text{MnO}_2$ -based carbon composites [35]. The XRD pattern of the  $\text{MnO}_2$ -NPs was attributed to the monoclinic potassium birnessite, which was composed of 2D edge-shared  $\text{MnO}_6$  octahedral layers with  $\text{K}^+$  and  $\text{H}_2\text{O}$  molecules contained in the interlayer space [4].



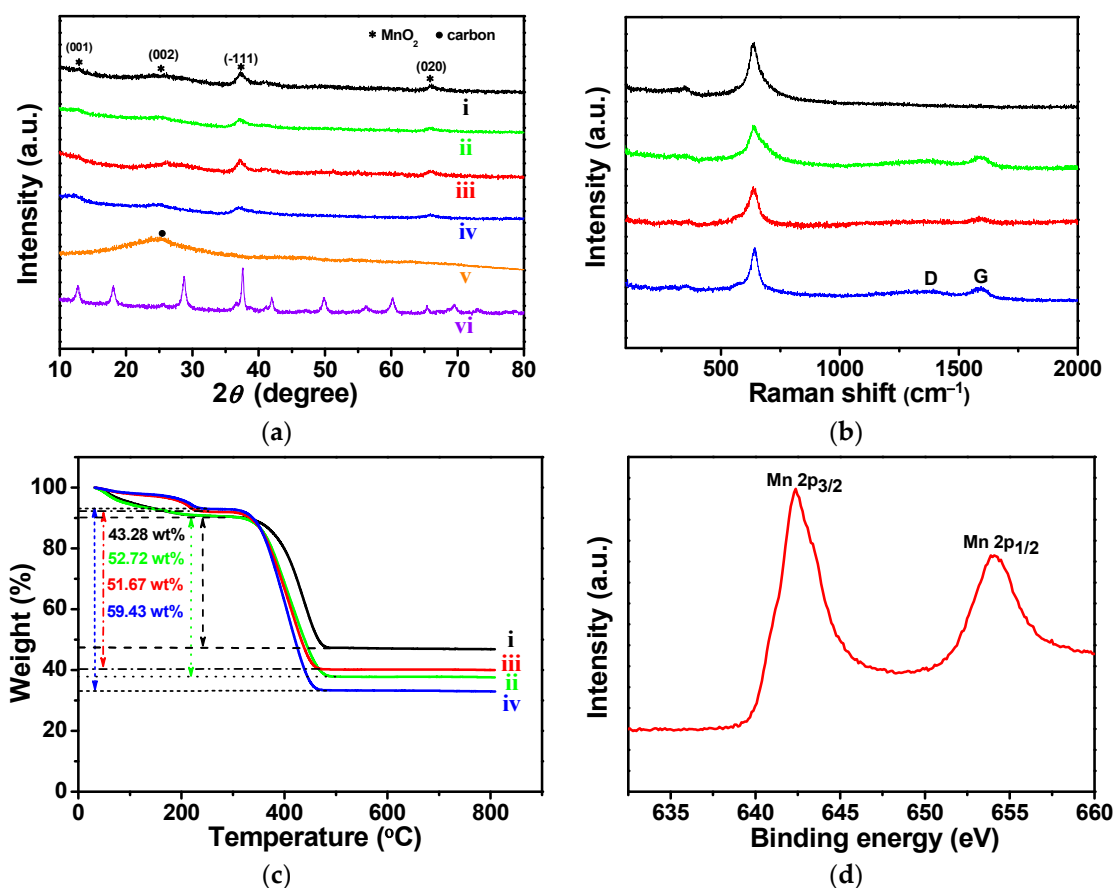


**Figure 5.** (a) X-ray diffraction patterns, (b) Raman spectra and (c) TGA curves of the samples. Curve i: MnO<sub>2</sub>-TiO<sub>2</sub>-carbon-47.28%; curve ii MnO<sub>2</sub>-TiO<sub>2</sub>-carbon-37.81%; curve iii MnO<sub>2</sub>-carbon-40.15%; curve iv: MnO<sub>2</sub>-carbon-33.30%; curve v: TiO<sub>2</sub>-carbon; curve vi: MnO<sub>2</sub>-NPs. (d) High-resolution XPS spectra of Mn 2p regions of the MnO<sub>2</sub>-TiO<sub>2</sub>-carbon-47.28% composite.

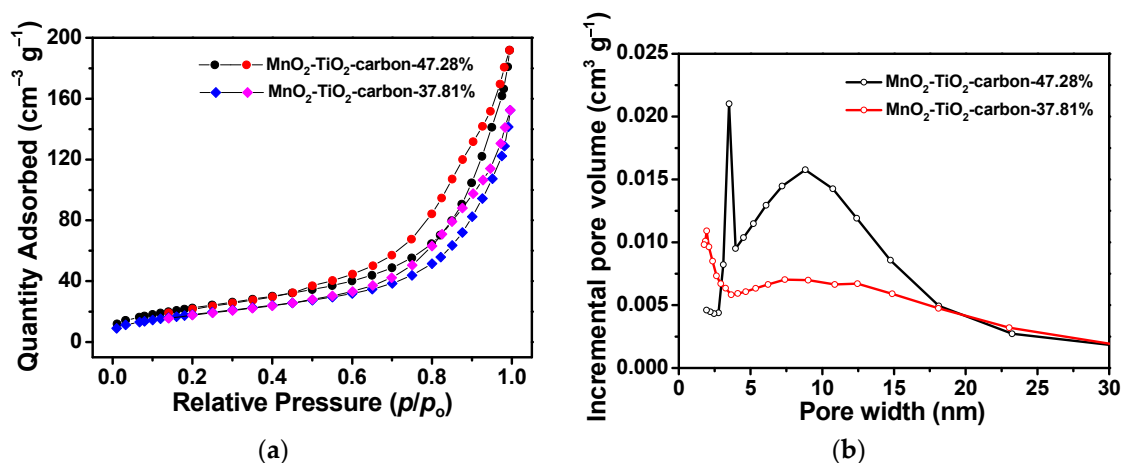
The structure features of the MnO<sub>2</sub>-TiO<sub>2</sub>-carbon composites were further verified using Raman spectra, as shown in Figure 5b. A broad peak located around 650 cm<sup>-1</sup> was assigned to the Mn-O stretching vibration of the MnO<sub>6</sub> octahedra [33]. Two weak peaks positioned at 1350 and 1590 cm<sup>-1</sup> were ascribed to the D- and G-bands of the carbon materials, respectively [36]. The corresponding peak intensities of the D- and G-bands of carbon components became lower with the increasing content of MnO<sub>2</sub> nanosheets in the MnO<sub>2</sub>-TiO<sub>2</sub>-carbon and MnO<sub>2</sub>-carbon composites, which was due to the depletion of carbon during the formation of the MnO<sub>2</sub> nanosheets (Equation (1)). However, the TiO<sub>2</sub> peaks could not be clearly identified in the MnO<sub>2</sub>-TiO<sub>2</sub>-carbon-47.28% and 37.81% materials because there was less TiO<sub>2</sub> content, and they are almost completely covered by intensively immobilized MnO<sub>2</sub> nanosheets [32].

The carbon and MnO<sub>2</sub> contents in the resultant MnO<sub>2</sub>-based carbon composites were evaluated using TGA measurements. As exhibited in Figure 5c, below 250 °C, about 8–10 wt % weight loss of the samples occurred due to the evaporation of water and other small molecules. Rapid weight losses during the oxidation of the carbon nanofibers between 300–500 °C in air were calculated as 43.28, 52.72, 51.67 and 59.43 wt % for the MnO<sub>2</sub>-TiO<sub>2</sub>-carbon-47.28%, 37.81% and MnO<sub>2</sub>-carbon-40.15%, 33.30%, respectively. Moreover, the contents of TiO<sub>2</sub> were too low and could be ignored in the two titania-based composites. Thus, the contents of MnO<sub>2</sub> contained in the MnO<sub>2</sub>-TiO<sub>2</sub>-carbon-47.28%, 37.81% and MnO<sub>2</sub>-carbon-40.15%, 33.30% are 47.28, 37.81, 40.15 and 33.30 wt %, respectively.

The Mn 2p peaks from the XPS spectrum were tested to study the valence state of Mn in the MnO<sub>2</sub>-TiO<sub>2</sub>-carbon-47.28% composite, and the results are shown in Figure 5d. Two peaks centered at 653.8 and 642.1 eV were indexed to Mn 2p<sub>1/2</sub> and Mn 2p<sub>3/2</sub>, re-

spectively. The energy separation value of 11.7 eV is well in accordance with the known data for  $\text{MnO}_2$  [37]. Moreover, the oxidation state of Mn in the  $\text{MnO}_2$ - $\text{TiO}_2$ -carbon-37.81% composite showed the similar results to those of  $\text{MnO}_2$ - $\text{TiO}_2$ -carbon-47.28% composite, which demonstrated the existence of  $\text{MnO}_2$  in the sample (Figure S4).

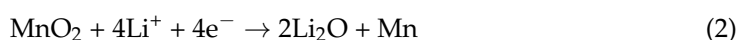
Figure 6 displays the  $\text{N}_2$  adsorption–desorption isotherms and the pore-size distribution curves of the  $\text{MnO}_2$ - $\text{TiO}_2$ -carbon-47.28%, -37.81% composites. Both of the composite materials clearly show type IV isotherms with a type H3 hysteresis loop, indicating the existence of mesopores in the composites [38]. The specific surface areas of the  $\text{MnO}_2$ - $\text{TiO}_2$ -carbon-47.28% and 37.81% were 83.2 and 67.1  $\text{m}^2 \text{g}^{-1}$  (Figure 6a), and the pore volumes of the two composites were calculated to be 0.299 and 0.238  $\text{cm}^3 \text{g}^{-1}$ , respectively. A mesoporous structure was observed for the  $\text{MnO}_2$ - $\text{TiO}_2$ -carbon-47.28% composite with average sizes of 3.5 and 8.8 nm (Figure 6b). However, the average pore size of the  $\text{MnO}_2$ - $\text{TiO}_2$ -carbon-37.81% was measured to be 1.9 nm. Due to the larger specific surface area and the mesoporous structure of the  $\text{MnO}_2$ - $\text{TiO}_2$ -carbon-47.28% composite, this material could supply sufficient active sites and accelerate electron transportation during  $\text{Li}^+$  insertion/extraction processes, thus leading to better electrochemical performance of the electrode material. Hence, it is concluded that the composite with a larger pore volume and higher specific surface area is able to deliver a high specific capacity and long cycling life during the charge/discharge processes [31].



**Figure 6.** (a) Nitrogen adsorption–desorption isotherms and the (b) pore-size distribution curves of the  $\text{MnO}_2$ - $\text{TiO}_2$ -carbon-47.28% and  $\text{MnO}_2$ - $\text{TiO}_2$ -carbon-37.81% composites.

### 3.2. Electrochemical Study of the $\text{MnO}_2$ - $\text{TiO}_2$ -Carbon and $\text{MnO}_2$ -Carbon Composites

The electrochemical performances of the nanofibrous  $\text{MnO}_2$ - $\text{TiO}_2$ -carbon composites employed as anodic materials for LIBs were tested to evaluate the kinetics of  $\text{Li}^+$  intercalation/deintercalation processes. Figure 7 shows the cyclic voltammetric (CV) curves of  $\text{MnO}_2$ - $\text{TiO}_2$ -carbon-47.28%,  $\text{MnO}_2$ -carbon-40.15% and  $\text{MnO}_2$ -NPs electrodes during charge/discharge processes in the voltage range from 0.01 to 3.0 V with a scan rate of 0.2  $\text{mV s}^{-1}$ . In the initial cathodic curves of both  $\text{MnO}_2$ - $\text{TiO}_2$ -carbon-47.28% and  $\text{MnO}_2$ -carbon-40.15% electrodes (Figure 7a,b), a broad peak centered at 0.1 V was attributed to the formation of a solid–electrolyte interface (SEI) layer and a reduction of  $\text{Mn}^{2+}$  to metallic  $\text{Mn}^0$  [16], and two mild peaks at 1.17 and 2.46 V corresponded to the reduction of  $\text{MnO}_2$  to  $\text{Mn}^{2+}$  and the decomposition of electrolytes [19,39]. The whole discharge process was calculated as Equation (2):



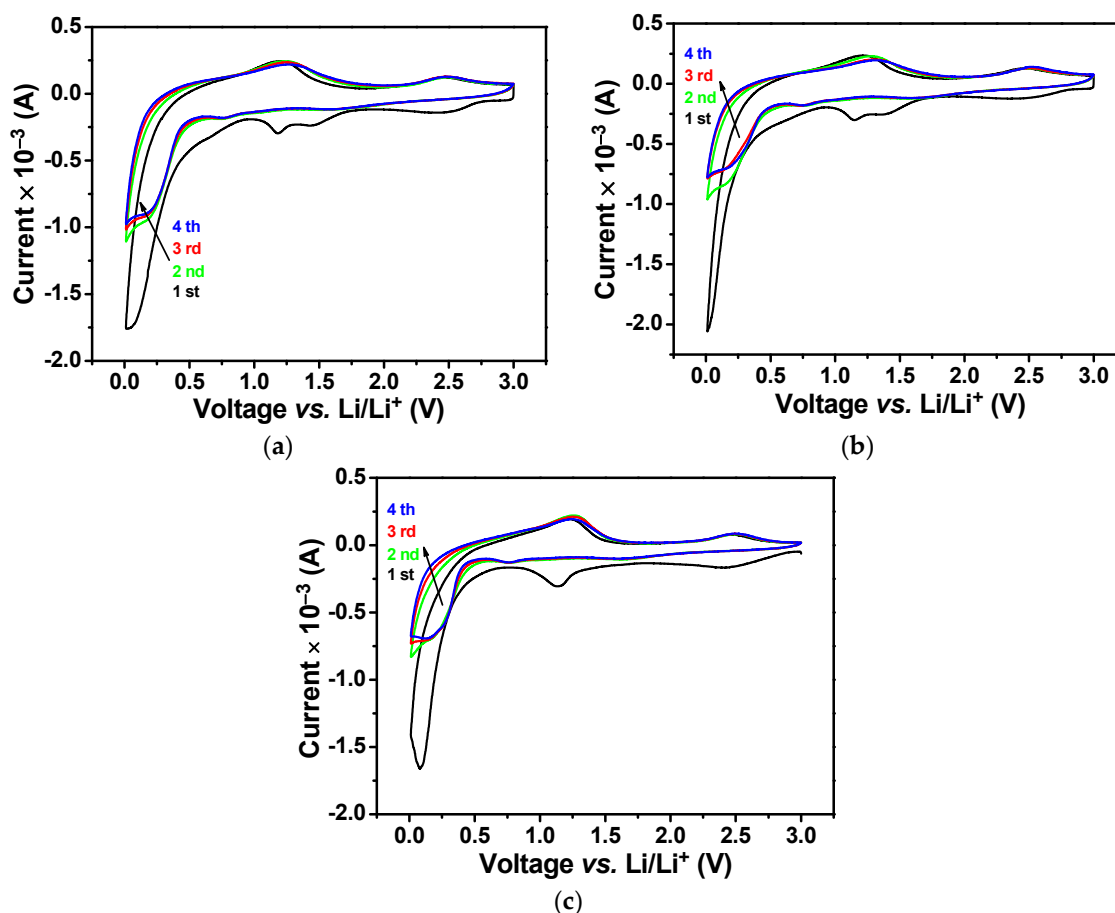
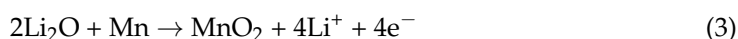


**Figure 7.** Cyclic voltammetry curves of (a) MnO<sub>2</sub>-TiO<sub>2</sub>-carbon-47.28%, (b) MnO<sub>2</sub>-carbon-40.15% composite and (c) MnO<sub>2</sub>-NPs tested in the initial four charge/discharge cycles at a scan rate of 0.2 mV s<sup>-1</sup> between 0.01 and 3 V (vs. Li/Li<sup>+</sup>).

Two oxidation peaks at 1.24 and 2.45 V were observed in the first anodic curve, which were attributed to the oxidations of Mn<sup>0</sup> to Mn<sup>2+</sup> and Mn<sup>2+</sup> to Mn<sup>4+</sup>, respectively [39]. The whole charge process was calculated as Equation (3):



In the next cycles, the reduction peak at 0.1 V and the oxidation peak at 1.18 V shifted to 0.15 and 1.24 V, respectively. The distinct shifts in the subsequent cycles were attributed to the structural changes and reconstitutions initiated by the formation of amorphous Li<sub>2</sub>O and Mn<sup>0</sup> [40–43]. For MnO<sub>2</sub>-NPs, an acuminate cathodic peak centered at 0.08 V and a relatively weaker peak at 1.14 V in the first charge curve were ascribed to the formation of a SEI layer and the reduction of MnO<sub>2</sub> to Mn (Figure 7c). Two oxidation peaks at 1.24 and 2.47 V were noticed in the charge curves, which meant a two-step electrochemical reaction [19]. The weak redox peaks in the first cycles of the three anodes located at 0.67 and 2.47 V were attributed to the conversion reaction between the Cu metal (copper foam) and CuO, and the Cu<sub>2</sub>O hybrid nanocomposite, and the cathodic peak shift to 0.76 V in subsequent cycles [44]. The peak intensities of the CV curves of MnO<sub>2</sub>-carbon-40.15% and MnO<sub>2</sub>-NPs decreased over the next three charge/discharge cycles, indicating fading of the irreversible capacity of the first cycle. In comparison, the peak intensities of the curves (Figure 7a) overlapped well in the next three cycles, implying excellent electrochemical reversibility and the structural stability of the MnO<sub>2</sub>-TiO<sub>2</sub>-carbon-47.28% anode. The ultra-thin titania film coating layer served as a protective barrier during the reaction of MnO<sub>4</sub><sup>-</sup> with carbon nanofiber and led to the uniform immobilization of MnO<sub>2</sub> nanosheets with higher contents, which was well in accordance with the TGA measurements. The CV curves

of the MnO<sub>2</sub>-TiO<sub>2</sub>-carbon-37.81% and MnO<sub>2</sub>-carbon-33.30% anodes showed similar peak shifts as MnO<sub>2</sub>-TiO<sub>2</sub>-carbon-47.28% and MnO<sub>2</sub>-carbon-40.15%, implying analogous Li<sup>+</sup> insertion/extraction processes (Figure S5). However, the intensities of the charge/discharge curves decreased quickly in subsequent cycles, indicating that the fast irreversible capacity was fading and that there was poor cycling stability.

The charge/discharge curves of the MnO<sub>2</sub>-TiO<sub>2</sub>-carbon-47.28%, MnO<sub>2</sub>-carbon-40.15%, TiO<sub>2</sub>-carbon nanofiber and MnO<sub>2</sub>-NPs electrodes are shown in Figure 8. The first discharge and charge capacities of MnO<sub>2</sub>-TiO<sub>2</sub>-carbon-47.28% composite were 1341 and 547 mAh g<sup>-1</sup> (Figure 8a), respectively, showing a Coulombic efficiency of 41%. The huge irreversible capacity degradation was due to the formation of a SEI layer that covered the surface of the electrode material [45]. In following cycles, the charge/discharge capacities of the electrode materials were reduced from 556 to 489 mAh g<sup>-1</sup> as they cycled to the 5th cycle. The Coulombic efficiency increased to 98% at the 10th cycle, the cycling capacities continued to slowly rise and finally reached a constant capacity of 652 mAh g<sup>-1</sup> by the 100th cycle. A flat voltage plateau at around 0.4–0.5 V during the discharge process indicated the reduction of MnO<sub>2</sub> to Mn in one step. However, a sharp plateau and a short plateau were observed in following discharge processed, implying two steps of reduction of Li with MnO<sub>2</sub>. Two charge plateaus at around 1.0–1.3 V and 2.2–2.5 V demonstrated the oxidation of Mn<sup>0</sup> in two steps [33,46]. These results are well in accordance with the CV measurements. As a comparison, the MnO<sub>2</sub>-TiO<sub>2</sub>-carbon-37.81% electrode exhibited discharge and charge capacities of 1259 and 477 mAh g<sup>-1</sup>, respectively, resulting in a Coulombic efficiency of 37.9%. Moreover, the discharge capacity fell to 407 mAh g<sup>-1</sup> after 10 cycles and slowly increased to a stable capacity of 494 mAh g<sup>-1</sup> by the 100th cycle (Figure S6a). The MnO<sub>2</sub>-TiO<sub>2</sub>-carbon-47.28% composite showed better electrochemical performance than MnO<sub>2</sub>-TiO<sub>2</sub>-carbon-37.81%, and its charge/discharge plateaus were longer, which implied well-organized MnO<sub>2</sub> nanosheets with higher contents in the composite-47.28% electrode that furnished adequate active sites for the Li<sup>+</sup> and electron transport. The discharge capacities of MnO<sub>2</sub>-carbon-40.15% electrodes dropped rapidly from 1251 to 367 mAh g<sup>-1</sup> when cycled for 20 cycles (Figure 8b). The large capacity loss of the MnO<sub>2</sub>-carbon-40.15% electrode was related to the weak adhesion between the MnO<sub>2</sub> nanosheets and the carbon nanofiber, thus leading to the exfoliation and structure destruction of MnO<sub>2</sub> during cycling. As for the MnO<sub>2</sub>-carbon-33.30% electrodes, the primary discharge and charge capacities of the composite were 1053 and 386 mAh g<sup>-1</sup>, respectively, presenting a Coulombic efficiency of 36.7% (Figure S6b). The severe capacity degradation of the MnO<sub>2</sub>-carbon-33.30% was attributed to the weak adhesion between the MnO<sub>2</sub> nanosheets and carbon nanofibers that led to the debonding of MnO<sub>2</sub> nanosheets from the carbon nanofibers. These exfoliated MnO<sub>2</sub> nanosheets may have suffered from huge volume changes and lost their effective contact with the electrolyte, resulting in the poor electrochemical performance of the electrodes [34]. The discharge capacity the TiO<sub>2</sub>-carbon nanofibers decreased from 985 to 249 mAh g<sup>-1</sup> after 100 cycles (Figure 8c). This further demonstrated that the immobilized MnO<sub>2</sub> nanosheets significantly boosted the capacity of MnO<sub>2</sub>-TiO<sub>2</sub>-carbon composites and improved the structure stability of the electrodes during the Li<sup>+</sup> intercalation/deintercalation processes. However, the initial discharge and charge capacities of MnO<sub>2</sub>-NPs were 1276 and 464 mAh g<sup>-1</sup>, respectively, giving a Coulombic efficiency of 36.4% (Figure 8d), and the capacity steadily decreased to 146 mAh g<sup>-1</sup> after 100 cycles. The great irreversible capacity loss was ascribed to the aggregation and pulverization of MnO<sub>2</sub>-NPs during the repeated charge/discharge processes, thus leading to poor cycling stability as well as a low rate capability.

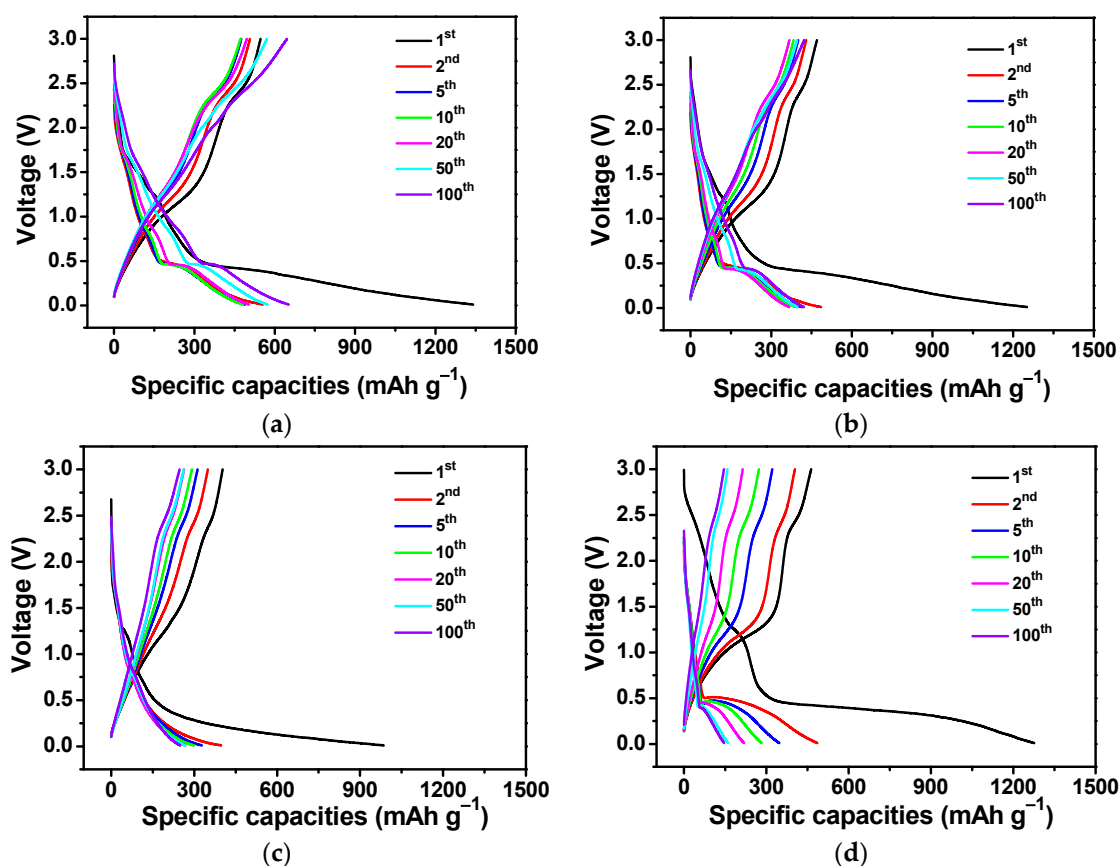


**Figure 8.** Galvanostatic charge/discharge profiles of (a) MnO<sub>2</sub>-TiO<sub>2</sub>-carbon-47.28%, (b) MnO<sub>2</sub>-carbon-40.15%, (c) TiO<sub>2</sub>-carbon and (d) MnO<sub>2</sub>-NPs anode materials measured at a current density of 100 mA g<sup>-1</sup> between 0.01 and 3.0 V.

The cycling performance of the MnO<sub>2</sub>-TiO<sub>2</sub>-carbon-47.28%, 37.81%, MnO<sub>2</sub>-carbon-40.15%, 33.30%, TiO<sub>2</sub>-carbon nanofibers and MnO<sub>2</sub>-NPs are shown in Figure 9a. For the MnO<sub>2</sub>-TiO<sub>2</sub>-carbon-47.28% composite, the capacity dropped rapidly in the first three cycles and thereafter increased gradually after 10 cycles, reaching a capacity of 677 mAh g<sup>-1</sup> by the 130th cycle, delivering a Coulombic efficiency of over 99%. The reason for the improvement in capacity has been elucidated for many transition metal oxides, which might be attributed to the reversible growth of the polymeric gel-like film and the activation of electrode materials during Li<sup>+</sup> insertion/extraction processes [46–48]. A variety of reported MnO<sub>2</sub> nanostructures and MnO<sub>2</sub>-based composites have turned out to be good anode materials for LIBs [18,33,34,49–51]. The present fabricated bio-inspired nanofibrous MnO<sub>2</sub>-TiO<sub>2</sub>-carbon-47.28% composite showed comparable or better capacity capability when tested at identical current densities (Table 1). These enhancements were ascribed to the three-dimensional reticular structure and the high surface-to-volume ratio of the composite derived from the natural cellulosic substances, which effectively alleviated the large volume expansion and exfoliation of the MnO<sub>2</sub> nanosheets. Therefore, the MnO<sub>2</sub>-TiO<sub>2</sub>-carbon-47.28% electrode material exhibited superior electrochemical performance during cycling. However, the MnO<sub>2</sub>-TiO<sub>2</sub>-carbon-37.81%, with a relative lower content of MnO<sub>2</sub>, showed a stable capacity of 491 mAh g<sup>-1</sup> after 130 cycles, implying that the higher MnO<sub>2</sub> loading is capable of contributing a larger capacity to the composites. As a comparison, the capacity of MnO<sub>2</sub>-carbon-40.15% faded sharply in the initial 20 cycles and a steady capacity of 425 mAh g<sup>-1</sup> was obtained after 130 charge/discharge cycles. The capacity difference among the MnO<sub>2</sub>-TiO<sub>2</sub>-carbon and MnO<sub>2</sub>-carbon-40.15% composites suggested that the ultrathin titania film pre-coated on the surface of the carbon nanofibers plays an important role in improving the stability of the cycling performance of the electrodes. It was found that the TiO<sub>2</sub> coating layer facilitated the growth of well-organized MnO<sub>2</sub> nanosheets with

a higher content in the case of the  $\text{KMnO}_4$  precursor with a high concentration is used. While the discharge capacity of  $\text{MnO}_2$ -carbon-33.30% dropped from 1053 to 335  $\text{mAh g}^{-1}$  after 130 cycles. This further illustrated that  $\text{MnO}_2$  nanosheets were likely to be peeled off from the composite and tended to aggregate during  $\text{Li}/\text{Li}^+$  processes, thus leading to severe capacity fading. The  $\text{TiO}_2$ -carbon nanofibers delivered a fast capacity loss in the first 20 cycles and slowly decreased to 235  $\text{mAh g}^{-1}$  by the 130th cycle, corresponding to a 58.5% retention of the first charge capacity. The large irreversible capacity degradation of the electrode was ascribed to the formation of a SEI layer. For the  $\text{MnO}_2$ -NPs, a sudden capacity loss was observed in the initial 30 cycles and then slowly reduced to 145  $\text{mAh g}^{-1}$  at the 130th cycle, resulting in a capacity retention of 29.8% for the second discharge capacity. This phenomenon can be explained by the huge volume expansion and aggregation of  $\text{MnO}_2$ -NPs during the electrochemical processes.

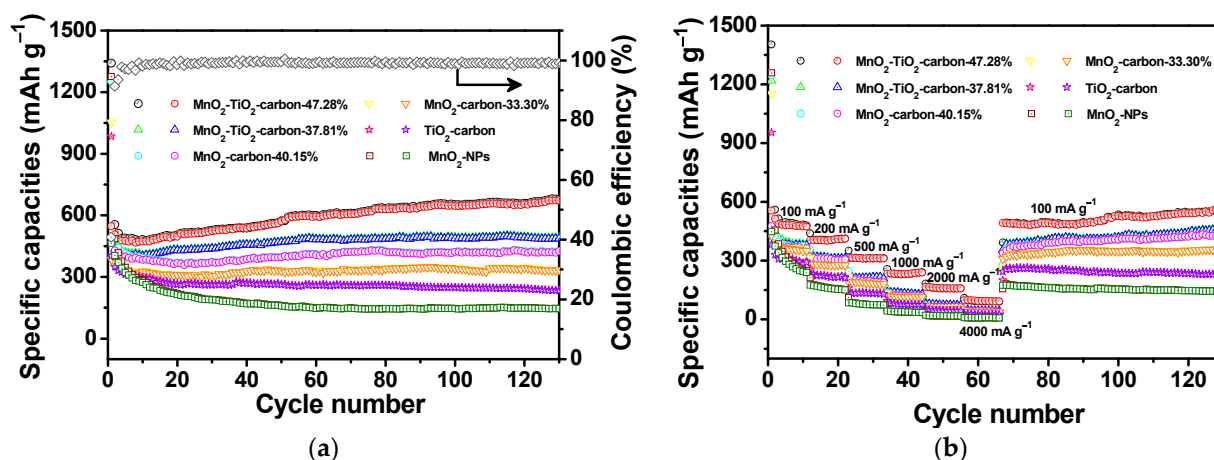


**Figure 9.** (a) Cycling performances of  $\text{MnO}_2$ - $\text{TiO}_2$ -carbon-47.28%, 37.81%,  $\text{MnO}_2$ -carbon-40.15%, 33.30% composites,  $\text{TiO}_2$ -carbon and  $\text{MnO}_2$ -NPs electrodes at a current density of  $100 \text{ mA g}^{-1}$  as well as the Coulombic efficiency curve of the  $\text{MnO}_2$ - $\text{TiO}_2$ -carbon-47.28% composite. (b) Rate performances of the corresponding electrodes at various current rates.

**Table 1.** The comparison of the electrochemical performances of the nanofibrous  $\text{MnO}_2$ - $\text{TiO}_2$ -carbon composite with other reported analogous  $\text{MnO}_2$ -based composites used as anodic materials for lithium-ion batteries.

Materials	Electrolyte	Current Density ( $\text{mA g}^{-1}$ )	Cycle Number	Capacity Retention ( $\text{mAh g}^{-1}$ )	Refs.
Pine-like $\alpha$ - $\text{MnO}_2$	EC:DMC = 1:1, (v/v)	100	150	381	[49]
$\text{TiO}_2$ nanotube arrays@ $\text{MnO}_2$ nanosheet	EC:EMC:DMC = 1:1:1, (v/v/v)	700	100	320	[50]
Coaxial $\text{MnO}_2$ /Carbon Nanotube Array	EC:DMC = 1:1, (v/v)	50	15	500	[18]
Nanoflake $\text{MnO}_2$ /carbon nanotube	EC:DEC = 1:1, (v/v)	200	50	620	[34]
$\text{TiO}_2$ -C/ $\text{MnO}_2$ nanowires	EC:DMC = 3:7, (v/v)	335	100	352	[33]
$\text{TiO}_2$ @C@ $\text{MnO}_2$ multi-shelled hollow nanospheres	EC:EMC:DMC = 1:1:1, (v/v/v)	100.5	100	506.8	[51]
Nanofibrous $\text{MnO}_2$ - $\text{TiO}_2$ -carbon	EC:EMC:DMC = 1:1:1, (v/v/v)	100	130	677	This work

To evaluate the capacity contribution of the  $\text{MnO}_2$  component to  $\text{MnO}_2$ - $\text{TiO}_2$ -carbon-47.28%, 37.81% and  $\text{MnO}_2$ -carbon-40.15%, 33.30% composites, the capacities of  $\text{MnO}_2$  were calculated using the following Equation (4):

$$C(\text{total}) = C_{(\text{TiO}_2/\text{carbon})} \times W_{(\text{carbon})} \text{ wt\%} + C_{(\text{MnO}_2)} \times W_{(\text{MnO}_2)} \text{ wt\%} \quad (4)$$

Since the  $\text{TiO}_2$  in the  $\text{MnO}_2$ - $\text{TiO}_2$ -carbon composite was too low and could be ignored, the separated capacity contribution of titania and carbon constituents in the electrodes were calculated as the whole capacity of the  $\text{TiO}_2$ -carbon. The results are listed in Table 2, where the contributed specific capacities of  $\text{MnO}_2$  in the  $\text{MnO}_2$ - $\text{TiO}_2$ -carbon-47.28%, 37.81%,

MnO<sub>2</sub>-carbon-40.15%, 33.30% electrodes were 1169.9, 912.5, 708.2, 535.3 mAh g<sup>-1</sup>, respectively. The contribution percentages of MnO<sub>2</sub> were equivalent to 95.1%, 74.2%, 57.6%, and 43.5% of the theoretical capacity (1230 mAh g<sup>-1</sup>), respectively. Significant improvements to the contributing capacity and percentage of MnO<sub>2</sub> in the MnO<sub>2</sub>-TiO<sub>2</sub>-carbon-47.28% electrode were ascribed to its three-dimensionally interwoven structures with its large specific area, which enabled faster Li<sup>+</sup> and electron transport during the electrochemical processes. Moreover, the mesoporous structure with a higher content of MnO<sub>2</sub> nanosheets in the composite made a large contribution to the enhancement of the capacity. Therefore, the MnO<sub>2</sub>-TiO<sub>2</sub>-carbon-47.28% composite showed superior cycling stability and a high specific capacity when compared with the other three MnO<sub>2</sub>-based counterparts.

**Table 2.** Comparisons of the contributed capacities and percentages of MnO<sub>2</sub> to the theoretical capacities in the MnO<sub>2</sub>-TiO<sub>2</sub>-carbon-47.28%, 37.81%, (sample-47.28%, -37.81%), and MnO<sub>2</sub>-carbon-40.15%, 33.30% (sample-40.15%, -33.30%), TiO<sub>2</sub>-carbon and MnO<sub>2</sub>-NPs electrodes.

Samples	Content of MnO <sub>2</sub> (wt %)	Content of TiO <sub>2</sub> -Carbon (wt %)	Total Capacity of Electrode after 130 Cycles (mAh g <sup>-1</sup> )	Contributed Capacity of MnO <sub>2</sub> in the Electrode (mAh g <sup>-1</sup> )	Contribution Percentage of MnO <sub>2</sub> to the Theoretical Capacity (%)
sample-47.28%	47.28	52.72	677	1169.9	95.1
sample-37.81%	37.81	62.12	491	912.5	74.2
sample-40.15%	40.15	59.85	425	708.2	57.6
sample-33.30%	33.30	66.70	335	535.3	43.5
TiO <sub>2</sub> -carbon	—	~100	235	—	—
MnO <sub>2</sub> -NPs	~100	—	145	145	11.8

To further investigate the electrochemical superiority of the MnO<sub>2</sub>-TiO<sub>2</sub>-carbon-47.28% composite, the rate performances of the composite electrodes at varied current rates are shown in Figure 9b. The MnO<sub>2</sub>-TiO<sub>2</sub>-carbon-47.28% electrode delivered discharge-specific capacities of 491, 406, 312, 232, 158, and 94 mAh g<sup>-1</sup> with current densities increasing from 100, 200, 500, 1000, 2000, and 4000 mA g<sup>-1</sup>, respectively. When the current rate was set back to 100 mA g<sup>-1</sup>, a reversible capacity of 493 mAh g<sup>-1</sup> was obtained and successively increased to 560 mAh g<sup>-1</sup>, implying the favorable rate capabilities of the electrode. In the meantime, the rate capability of MnO<sub>2</sub>-TiO<sub>2</sub>-carbon-37.81% was slightly higher than that of the MnO<sub>2</sub>-carbon-40.15%, and the discharge capacities of composite-37.81% were 392, 319, 212, 132, 73, and 44 mAh g<sup>-1</sup> at current rates of 100, 200, 500, 1000, 2000, and 4000 mA g<sup>-1</sup>, respectively. However, the specific capacities of the MnO<sub>2</sub>-carbon-40.15% electrode were 376, 313, 194, 120, 61, and 41 mAh g<sup>-1</sup> at comparable current densities for composite-37.81%. Though the content of MnO<sub>2</sub> in the MnO<sub>2</sub>-TiO<sub>2</sub>-carbon-37.81% was lower than that of MnO<sub>2</sub>-carbon-40.15%, the composite-37.81% still displayed a better rate capability than composite-40.15%. It was concluded that the structural stability of the composite and the strong adhesion of MnO<sub>2</sub> nanosheets to the titania film pre-coated carbon nanofibers greatly prevented the exfoliation and pulverization of MnO<sub>2</sub> in MnO<sub>2</sub>-TiO<sub>2</sub>-carbon-37.81%, and led to a superior rate performance. The MnO<sub>2</sub>-carbon-33.30% anode showed lower specific capacities of 368, 281, 184, 115, 56, 37, and 330 mAh g<sup>-1</sup> at the current rates of 100, 200, 500, 1000, 2000, and 4000 mA g<sup>-1</sup>, respectively. A reversible capacity of 330 mAh g<sup>-1</sup> was retained when the current rate returned to 100 mA g<sup>-1</sup>. The MnO<sub>2</sub>-carbon-33.30% electrode exhibited a poor rate performance because of less loading content of MnO<sub>2</sub> nanosheets, as well as the weak force between the carbon nanofibers and the MnO<sub>2</sub>, resulting in the structural destruction of active materials. As for the TiO<sub>2</sub>-carbon nanofibers, the specific capacities were obviously lower than those of the four MnO<sub>2</sub>-based samples mentioned above. In comparison, the specific capacity of MnO<sub>2</sub>-NPs decreased sharply in the initial 10 cycles. When the current rate was set in the range of 500–4000 mA g<sup>-1</sup>, the capacity reduced to as low as 10 mAh g<sup>-1</sup>. An irreversible capacity of 167 mAh g<sup>-1</sup> was acquired when the cycling density returned to 100 mA g<sup>-1</sup>. This further demonstrated that the severe volume expansion and aggregation of MnO<sub>2</sub>-NPs during the Li<sup>+</sup> intercalation/deintercalation processes are the main cause of the poor rate capability of the electrode.

To better understand the greatly enhanced electrochemical performances of the  $\text{MnO}_2$ - $\text{TiO}_2$ -carbon-47.28% electrode, electrochemical impedance spectroscopy (EIS) measurements were tested to compare the conductivity of the prepared  $\text{MnO}_2$ - $\text{TiO}_2$ -carbon-47.28%,  $\text{MnO}_2$ -carbon-40.15% and  $\text{TiO}_2$ -carbon electrodes after 200 repeated cycles. Nyquist plots of the three electrodes as shown in Figure 10 and depict a semicircle in the high frequency zone and an inclined line in the low-frequency region, corresponding to the charge transfer resistance and the Li ion diffusion activity, respectively. The kinetic parameters were evaluated using the equivalent circuit (inset in Figure 10), and  $R_s$  represents the internal resistance of the battery,  $R_{ct}$  is the charge transfer impedance on the electrode-electrolyte interface,  $W$  is the Warburg impedance of  $\text{Li}^+$  diffusion throughout the active materials, and CPE is the constant phase-angle element [35,52]. The fitting results are listed in Table S1, although the  $R_s$  values of the  $\text{MnO}_2$ - $\text{TiO}_2$ -carbon-47.28%,  $\text{MnO}_2$ -carbon-40.15% and  $\text{TiO}_2$ -carbon electrodes showed little difference, the values of  $R_{ct}$  of the three composite electrodes were measured to be 46.32, 155, and 231.7  $\Omega$ , respectively. The  $\text{MnO}_2$ - $\text{TiO}_2$ -carbon-47.28% had the lowest  $R_s$  and  $R_{ct}$  values; this strongly confirmed that the composite-47.28% had the lowest activation energy and underwent a fast charge transfer reaction, leading to a decrease on the internal resistance of the entire battery. In addition, the structural morphology property of the  $\text{MnO}_2$ - $\text{TiO}_2$ -carbon-47.28% electrode after 200 charge/discharge cycles was partially retained (Figure S7), demonstrating that structural stabilization was achieved and exhibited excellent cycling stability and reversible rate capability.

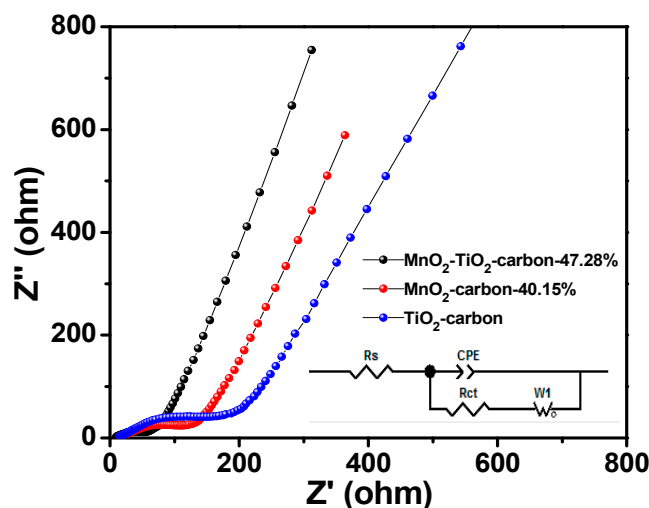


**Figure 10.** Electrochemical impedance spectra (Nyquist plots) of the  $\text{MnO}_2$ - $\text{TiO}_2$ -carbon-47.28%,  $\text{MnO}_2$ -carbon-40.15% and  $\text{TiO}_2$ -carbon electrodes after 200 charge/discharge cycles. The inset is the equivalent circuit model used to fit the impedance spectra.

#### 4. Conclusions

A cellulose substance-derived nanofibrous  $\text{MnO}_2$ - $\text{TiO}_2$ -carbon composite was fabricated by immobilizing porous  $\text{MnO}_2$  nanosheets on the surface of titania-coated carbon nanofibers employing a natural cellulose substance as both the carbon source and the structural matrix. The material, with a large surface area, faithfully inherited the three-dimensional network structures of the original cellulose substances. The  $\text{MnO}_2$ - $\text{TiO}_2$ -carbon-47.28% composite showed durable cycling performance and stable rate capabilities when employed as anodic materials for LIBs. The improved electrochemical performances of the  $\text{MnO}_2$ - $\text{TiO}_2$ -carbon-47.28% are attributed to the synergistic effect of the carbon nanofibers, the ultrathin titania coating layer, as well as the high content of  $\text{MnO}_2$  nanosheets. The internal carbon nanofibers act as a conductive matrix and facilitate Li ion and electron transfer during  $\text{Li}^+$  insertion/extraction processes. Moreover, the titania layer plays a key role in the higher loading of  $\text{MnO}_2$  nanosheets, and provides an intermediate interface for the strong adhesion between the carbon nanofiber and  $\text{MnO}_2$ . The mesoporous



MnO<sub>2</sub> nanosheets with a large theoretical specific capacity contribute to the higher capacity retention. The current method developed for the fabrication of bio-inspired electrode material provides a novel path for the introduction of sophisticated nanoarchitectures into energy-related fields.

**Supplementary Materials:** The following are available online at <https://www.mdpi.com/article/10.3390/ma14123411/s1>, Figure S1: Electron micrographs of the nanofibrous MnO<sub>2</sub>-TiO<sub>2</sub>-carbon-37.81% composite derived from the natural cellulose substance. (a) SEM image of the MnO<sub>2</sub>-TiO<sub>2</sub>-carbon-37.81% composite, (b) SEM image of an individual composite nanofiber isolated from the assemblies, (c,d) the TEM images of an individual MnO<sub>2</sub>-TiO<sub>2</sub>-carbon-37.81% nanofiber at different magnifications. Figure S2: Electron micrographs of the nanofibrous MnO<sub>2</sub>-carbon-33.30% composite derived from a natural cellulose substance. (a) SEM image of the MnO<sub>2</sub>-carbon-33.30% composite, (b) SEM and (c) TEM images of an individual composite nanofiber. Figure S3: (a,b) SEM and (c,d) TEM micrographs of the MnO<sub>2</sub>-NPs materials. Figure S4: The high-resolution XPS spectra of Mn 2p regions of the MnO<sub>2</sub>-TiO<sub>2</sub>-carbon-37.81% composite. Figure S5: Cyclic voltammetry curves of (a) MnO<sub>2</sub>-TiO<sub>2</sub>-carbon-37.81% and (b) MnO<sub>2</sub>-carbon-33.30% electrodes tested in the initial four charge/discharge cycles at a scan rate of 0.2 mV s<sup>-1</sup> between 0.01 and 3 V (vs. Li/Li<sup>+</sup>). Figure S6: Galvanostatic charge/discharge profiles of (a) MnO<sub>2</sub>-TiO<sub>2</sub>-carbon-37.81% and (b) MnO<sub>2</sub>-carbon-33.30% anode materials measured at a current density of 100 mA g<sup>-1</sup> between 0.01 and 3.0 V. Table S1: Equivalent circuit parameters obtained from fitting the experimental impedance spectra of the MnO<sub>2</sub>-TiO<sub>2</sub>-carbon-47.28%, MnO<sub>2</sub>-carbon-33.30 and TiO<sub>2</sub>-carbon nanocomposite electrodes. Figure S7: TEM image of the MnO<sub>2</sub>-TiO<sub>2</sub>-carbon-47.28% anode material after 200 charge/discharge cycles.

**Author Contributions:** Conceptualization, S.L.; methodology, S.L., M.Y., G.H., D.Q. and J.H.; investigation, S.L.; writing—original draft preparation, S.L.; writing—review and editing, S.L., M.Y., G.H., D.Q. and J.H.; supervision, J.H.; funding acquisition, S.L., J.H. All authors have read and agreed to the published version of the manuscript.

**Funding:** This research was funded by the Zhejiang Provincial Natural Science Foundation of China (LY16B010001, LQ20B030003).

**Institutional Review Board Statement:** Not applicable.

**Informed Consent Statement:** Not applicable.

**Data Availability Statement:** The data presented in this study are available on request from the corresponding author.

**Conflicts of Interest:** The authors declare no conflict of interest.

## References

1. Tarascon, J.-M.; Armand, M. Issues and challenges facing rechargeable lithium batteries. *Nature* **2001**, *414*, 359–367. [[CrossRef](#)] [[PubMed](#)]
2. Zeng, H.; Xing, B.; Zhang, C.; Chen, L.; Zhao, H.; Han, X.; Yi, G.; Huang, G.; Zhang, C.; Cao, Y. In situ synthesis of MnO<sub>2</sub>/porous graphitic carbon composites as high-capacity anode materials for lithium-ion batteries. *Energy Fuels* **2020**, *34*, 2480–2491. [[CrossRef](#)]
3. Pan, F.; Hou, S.; Wang, P.; Liu, M.; Luo, Y.; Zhao, L.  $\beta$ -MnO<sub>2</sub>/metal-organic framework derived nanoporous ZnMn<sub>2</sub>O<sub>4</sub> nanorods as lithium-ion battery anodes with superior lithium storage performance. *Chem. Eur. J.* **2019**, *25*, 5043–5050.
4. Cao, Z.; Yang, Y.; Qin, J.; Su, Z. A core-shell porous MnO<sub>2</sub>/Carbon nanosphere composite as the anode of lithium-ion batteries. *J. Power Sources* **2021**, *491*, 229577. [[CrossRef](#)]
5. Zhao, X.; Hayner, C.M.; Kung, M.C.; Kung, H.H. Flexible holey graphene paper electrodes with enhanced rate capability for energy storage applications. *ACS Nano* **2011**, *5*, 8739–8749. [[CrossRef](#)] [[PubMed](#)]
6. Poizot, P.; Laruelle, S.; Grugeon, S.; Dupont, L.; Tarascon, J.M. Nano-sized transition-metal oxides as negative-electrode materials for lithium-ion batteries. *Nature* **2000**, *407*, 496–499. [[CrossRef](#)]
7. Cao, Z.; Yang, Y.; Qin, J.; He, J.; Su, Z. Co<sub>3</sub>O<sub>4</sub> polyhedron@MnO<sub>2</sub> nanotube composite as anode for high-performance lithium-ion batteries. *Small* **2021**, *17*, 2008165. [[CrossRef](#)] [[PubMed](#)]
8. Anitha, T.; Reddy, A.E.; Vinodh, R.; Kim, H.-J.; Cho, Y.-R. Preparation and characterization of CoWO<sub>4</sub>/CoMn<sub>2</sub>O<sub>4</sub> nanoflakes composites on Ni foam for electrochemical supercapacitor applications. *J. Energy Storage* **2020**, *30*, 101483. [[CrossRef](#)]
9. Joo, H.-H.; Gopi, C.V.V.M.; Vinodh, R.; Kim, H.-J.; Sambasivam, S.; Obaidat, I.M. Facile synthesis of flexible and binder-free dandelion flower-like CuNiO<sub>2</sub> nanostructures as advanced electrode material for high-performance supercapacitors. *J. Energy Storage* **2019**, *26*, 100914. [[CrossRef](#)]

10. Kishore, S.C.; Atchudan, R.; Edison, T.N.J.I.; Perumal, S.; Alagan, M.; Vinodh, R.; Shanmugam, M.; Lee, Y.R. Solid waste-derived carbon fibers-trapped nickel oxide composite electrode for energy storage application. *Energy Fuels* **2020**, *34*, 14958–14967. [[CrossRef](#)]
11. Raman, V.; Mohan, N.V.; Balakrishnan, B.; Rajmohan, R.; Rajangam, V.; Selvaraj, A.; Kim, H.-J. Porous shiitake mushroom carbon composite with NiCo<sub>2</sub>O<sub>4</sub> nanorod electrochemical characteristics for efficient supercapacitor applications. *Ionics* **2020**, *26*, 345–354. [[CrossRef](#)]
12. Huyan, Y.; Chen, J.; Yang, K.; Zhang, Q.; Zhang, B. Tailoring carboxyl tubular carbon nanofibers/MnO<sub>2</sub> composites for high-performance lithium-ion battery anodes. *J. Am. Ceram. Soc.* **2021**, *104*, 1402–1414. [[CrossRef](#)]
13. Sui, Y.; Liu, C.; Zou, P.; Zhan, H.; Cui, Y.; Yang, C.; Cao, G. Polypyrrole coated δ-MnO<sub>2</sub> nanosheet arrays as a highly stable lithium-ion-storage anode. *Dalton Trans.* **2020**, *49*, 7903–7913. [[CrossRef](#)]
14. Han, Q.; Zhang, W.; Han, Z.; Wang, F.; Geng, D.; Li, X.; Li, Y.; Zhang, X. Preparation of PAN-based carbon fiber@MnO<sub>2</sub> composite as an anode material for structural lithium ion batteries. *J. Mater. Sci.* **2019**, *54*, 11972–11982. [[CrossRef](#)]
15. Zhang, H.; Du, X.; Ding, S.; Wang, Q.; Chang, L.; Ma, X.; Hao, X.; Pen, C. DFT calculations of the synergistic effect of λ-MnO<sub>2</sub>/graphene composites for electrochemical adsorption of lithium ions. *Phys. Chem. Chem. Phys.* **2019**, *21*, 8133–8140. [[CrossRef](#)] [[PubMed](#)]
16. Ee, S.J.; Pang, H.; Mani, U.; Yan, Q.; Ting, S.L.; Chen, P. An interwoven network of MnO<sub>2</sub> nanowires and carbon nanotubes as the anode for bendable lithium-ion batteries. *ChemPhysChem* **2014**, *15*, 2445–2449. [[CrossRef](#)]
17. Liu, L.; Shen, Z.; Zhang, X.; Ma, S. Facile controlled synthesis of MnO<sub>2</sub> nanostructures for high performance anodes in lithium-ion batteries. *J. Mater. Sci. Mater. Electron.* **2019**, *30*, 1480–1486. [[CrossRef](#)]
18. Reddy, A.L.M.; Shaijumon, M.M.; Gowda, S.R.; Ajayan, P.M. Coaxial MnO<sub>2</sub>/carbon nanotube array electrodes for high-performance lithium batteries. *Nano Lett.* **2009**, *9*, 1002–1006. [[CrossRef](#)]
19. Lai, H.; Li, J.; Chen, Z.; Huang, Z. Carbon nanohorns as a high-performance carrier for MnO<sub>2</sub> anode in lithium-ion batteries. *ACS Appl. Mater. Interfaces* **2012**, *4*, 2325–2328. [[CrossRef](#)]
20. Yu, A.; Park, H.W.; Davies, A.; Higgins, D.C.; Chen, Z.; Xiao, X. Free-standing layer-by-layer hybrid thin film of graphene-MnO<sub>2</sub> nanotube as anode for lithium ion batteries. *J. Phys. Chem. Lett.* **2011**, *2*, 1855–1860. [[CrossRef](#)]
21. Lin, Z.; Huang, J. Hierarchical nanostructures derived from cellulose for lithium-ion batteries. *Dalton Trans.* **2019**, *48*, 14221–14232. [[CrossRef](#)]
22. Wagemaker, M.; Kentgens, A.P.M.; Mulder, F.M. Equilibrium lithium transport between nanocrystalline phases in intercalated TiO<sub>2</sub> anatase. *Nature* **2002**, *418*, 397–399. [[CrossRef](#)]
23. Lin, Z.; Li, S.; Huang, J. Natural cellulose derived nanocomposites as anodic materials for lithium-ion batteries. *Chem. Rec.* **2020**, *20*, 187–208. [[CrossRef](#)]
24. Luo, Y.; Li, J.; Huang, J. Bioinspired hierarchical nanofibrous silver-nanoparticle/anatase-rutile-titania composite as an anode material for lithium-ion batteries. *Langmuir* **2016**, *32*, 12338–12343. [[CrossRef](#)]
25. Li, S.; Huang, J. A nanofibrous silver-nanoparticle/titania/carbon composite as an anode material for lithium ion batteries. *J. Mater. Chem. A* **2015**, *3*, 4354–4360. [[CrossRef](#)]
26. Xuan, M.; Zhao, J.; Shao, J.; Du, C.; Cui, W.; Duan, L.; Qi, W.; Li, J. Recent progresses in layer-by-layer assembled biogenic capsules and their applications. *J. Colloid Interface Sci.* **2017**, *487*, 107–117. [[CrossRef](#)] [[PubMed](#)]
27. Li, Q.; Jia, Y.; Dai, L.; Yang, Y.; Li, J. Controlled rod nanostructured assembly of diphenylalanine and their optical waveguide properties. *ACS Nano* **2015**, *9*, 2689–2695. [[CrossRef](#)] [[PubMed](#)]
28. Jia, Y.; Xuan, M.; Feng, X.; Duan, L.; Li, J.; Li, J. Reconstitution of motor proteins through molecular assembly. *Chin. J. Chem.* **2019**, *38*, 123–129. [[CrossRef](#)]
29. Tang, J.; Wang, J.; Shrestha, L.K.; Hossain, M.S.A.; Alothman, Z.A.; Yamauchi, Y.; Ariga, K. Activated porous carbon spheres with customized mesopores through assembly of diblock copolymers for electrochemical capacitor. *ACS Appl. Mater. Interfaces* **2017**, *9*, 18986–18993. [[CrossRef](#)]
30. Khan, A.H.; Ghosh, S.; Pradhan, B.; Dalui, A.; Shrestha, L.K.; Acharya, S.; Ariga, K. Two-dimensional (2D) nanomaterials towards electrochemical nanoarchitectonics in energy-related applications. *Bull. Chem. Soc. Jpn.* **2017**, *90*, 627–648. [[CrossRef](#)]
31. Lin, Z.; Li, S.; Huang, J. Natural cellulose substance based energy materials. *Chem. Asian J.* **2021**, *16*, 378–396. [[CrossRef](#)]
32. Li, S.; Wang, M.; Luo, Y.; Huang, J. Bio-inspired hierarchical nanofibrous Fe<sub>3</sub>O<sub>4</sub>-TiO<sub>2</sub>-carbon composite as a high-performance anode material for lithium-ion batteries. *ACS Appl. Mater. Interfaces* **2016**, *8*, 17343–17351. [[CrossRef](#)]
33. Liao, J.-Y.; Higgins, D.; Lui, G.; Chabot, V.; Xiao, X.; Che, Z. Multifunctional TiO<sub>2</sub>-C/MnO<sub>2</sub> core-double-shell nanowire arrays as high-performance 3D electrodes for lithium ion batteries. *Nano Lett.* **2013**, *13*, 5467–5473. [[CrossRef](#)] [[PubMed](#)]
34. Xia, H.; Lai, M.O.; Lu, L. Nanoflaky MnO<sub>2</sub>/carbon nanotube nanocomposites as anode materials for lithium-ion batteries. *J. Mater. Chem.* **2010**, *20*, 6896–6902. [[CrossRef](#)]
35. Li, L.; Raji, A.-R.O.; Tour, J.M. Graphene-wrapped MnO<sub>2</sub>-graphene nanoribbons as anode materials for high-performance lithium ion batteries. *Adv. Mater.* **2013**, *25*, 6298–6302. [[CrossRef](#)] [[PubMed](#)]
36. He, C.; Wu, S.; Zhao, N.; Shi, C.; Liu, E.; Li, J. Carbon encapsulated Fe<sub>3</sub>O<sub>4</sub> nanoparticles as a high-rate lithium ion battery anode material. *ACS Nano* **2013**, *7*, 4459–4469. [[CrossRef](#)] [[PubMed](#)]
37. Liu, D.; Zhang, Q.; Xiao, P.; Garcia, B.B.; Guo, Q.; Champion, R.; Cao, G. Hydrous manganese dioxide nanowall arrays growth and their Li<sup>+</sup> ions intercalation electrochemical properties. *Chem. Mater.* **2008**, *20*, 1376–1380. [[CrossRef](#)]

38. Xiao, W.; Chen, J.S.; Lu, Q.; Lou, X.W. Porous spheres assembled from polythiophene (PTh)-coated ultrathin MnO<sub>2</sub> nanosheets with enhanced lithium storage capabilities. *J. Phys. Chem. C* **2010**, *114*, 12048–12051. [[CrossRef](#)]
39. Chen, J.; Wang, Y.; He, X.; Xu, S.; Fang, M.; Zhao, X.; Shang, Y. Electrochemical properties of MnO<sub>2</sub> nanorods as anode materials for lithium ion batteries. *Electrochim. Acta* **2014**, *142*, 152–156. [[CrossRef](#)]
40. Wang, Z.; Luan, D.; Madhavi, S.; Hu, Y.; Lou, X.W. Assembling carbon-coated  $\alpha$ -Fe<sub>2</sub>O<sub>3</sub> hollow nanohorns on the CNT backbone for superior lithium storage capability. *Energy Environ. Sci.* **2012**, *5*, 5252–5256. [[CrossRef](#)]
41. Gu, X.; Chen, L.; Ju, Z.; Xu, H.; Yang, J.; Qian, Y. Controlled growth of porous  $\alpha$ -FeO branches on  $\beta$ -MnO nanorods for excellent performance in lithium-ion batteries. *Adv. Funct. Mater.* **2013**, *23*, 4049–4056. [[CrossRef](#)]
42. Sun, B.; Chen, Z.; Kim, H.-S.; Ahn, H.; Wang, G. MnO/C core-shell nanorods as high capacity anode materials for lithium-ion batteries. *J. Power Sources* **2011**, *196*, 3346–3349. [[CrossRef](#)]
43. Wu, M.-S.; Chiang, P.-C.J.; Lee, J.-T.; Lin, J.-C. Synthesis of manganese oxide electrodes with interconnected nanowire structure as an anode material for rechargeable lithium ion batteries. *J. Phys. Chem. B* **2005**, *109*, 23279–23284. [[CrossRef](#)]
44. Wang, X.; Tang, D.-M.; Li, H.; Yi, W.; Zhai, T.; Bando, Y.; Golberg, D. Revealing the conversion mechanism of CuO nanowires during lithiation-delithiation by in situ transmission electron microscopy. *Chem. Commun.* **2012**, *48*, 4812–4814. [[CrossRef](#)]
45. Zhang, J.; Huang, T.; Liu, Z.; Yu, A. Mesoporous Fe<sub>2</sub>O<sub>3</sub> nanoparticles as high performance anode materials for lithium-ion batteries. *Electrochem. Commun.* **2013**, *29*, 17–20. [[CrossRef](#)]
46. Yue, J.; Gu, X.; Chen, L.; Wang, N.; Jiang, X.; Xu, H.; Yang, J.; Qian, Y. General synthesis of hollow MnO<sub>2</sub>, Mn<sub>3</sub>O<sub>4</sub> and MnO nanospheres as superior anode materials for lithium ion batteries. *J. Mater. Chem. A* **2014**, *2*, 17421–17426. [[CrossRef](#)]
47. Grugeon, S.; Laruelle, S.; Dupont, L.; Tarascon, J.M. An update on the reactivity of nanoparticles Co-based compounds towards Li. *Solid State Sci.* **2003**, *5*, 895–904. [[CrossRef](#)]
48. Luo, W.; Hu, X.L.; Sun, Y.M.; Huang, Y.H. Controlled synthesis of mesoporous MnO/C networks by microwave irradiation and their enhanced lithium-storage properties. *ACS Appl. Mater. Interfaces* **2013**, *5*, 1997–2003. [[CrossRef](#)]
49. Sun, D.; Chen, J.; Yang, J.; Yan, X. Morphology and crystallinity-controlled synthesis of MnO<sub>2</sub> hierarchical nanostructures and their application in lithium ion batteries. *CrystEngComm* **2014**, *16*, 10476–10484. [[CrossRef](#)]
50. Zhu, Q.; Hu, H.; Li, G.; Zhu, C.; Yu, Y. TiO<sub>2</sub> Nanotube arrays grafted with MnO<sub>2</sub> nanosheets as high-performance anode for lithium ion battery. *Electrochim. Acta* **2015**, *156*, 252–260. [[CrossRef](#)]
51. Liu, L.; Peng, J.; Wang, G.; Ma, Y.; Yu, F.; Dai, B.; Guo, X.-H.; Wong, C.-P. Synthesis of mesoporous TiO<sub>2</sub>@C@MnO<sub>2</sub> multishelled hollow nanospheres with high rate capability and stability for lithium-ion batteries. *RSC Adv.* **2016**, *6*, 65243–65251. [[CrossRef](#)]
52. Wang, Q.; Zhang, D.-A.; Wang, Q.; Sun, J.; Xing, L.-L.; Xue, X.-Y. High electrochemical performances of  $\alpha$ -MoO<sub>3</sub>@MnO<sub>2</sub> core-shell nanorods as lithium-ion battery anodes. *Electrochim. Acta* **2014**, *146*, 411–418. [[CrossRef](#)]